Device

Article

Analysis and management of thermal loads generated *in vivo* by miniaturized optoelectronic implantable devices

Graphical abstract

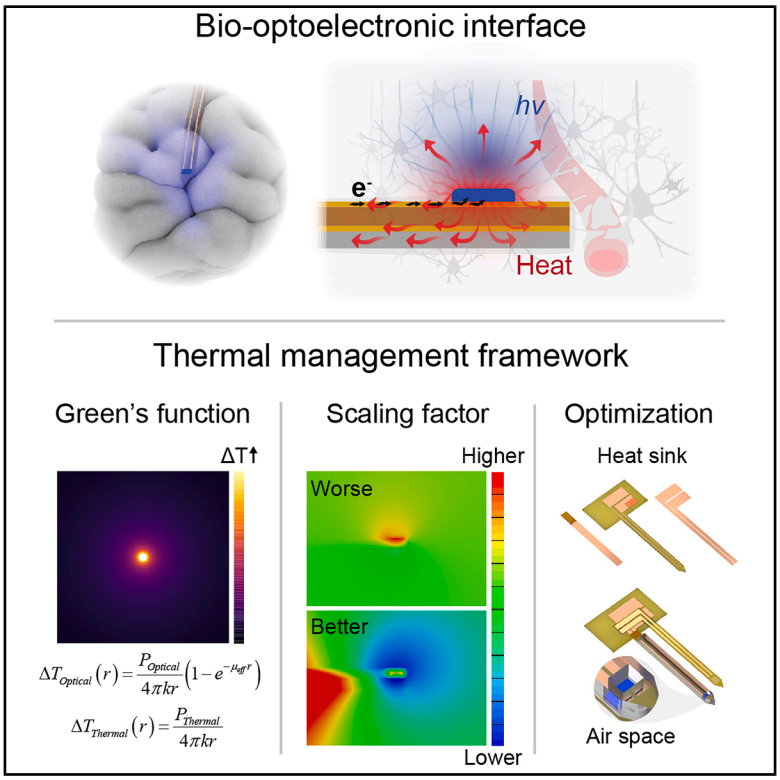

Highlights

- Generalizable framework for thermal management of implantable optoelectronics
- Green's function solves tissue heating from coupled thermal-optical sources
- Numerically modeled scaling factors enable comparison across device systems
- Analysis-guided device optimization reduces thermal load during brain stimulation

Authors

Mingzheng Wu, Kaiqing Zhang, Priscilla J. Y. Fok, ..., Abraham Vázquez-Guardado, Yonggang Huang, John A. Rogers

Correspondence

abraham.vg@ncsu.edu (A.V.-G.), y-huang@northwestern.edu (Y.H.), jrogers@northwestern.edu (J.A.R.)

In brief

Implantable optoelectronics offer precise stimulation and sensing capabilities, but managing heat generation remains a key challenge for both safety and performance. This study presents a generalizable framework that combines analytical solution, numerical modeling, and *in vivo* validation to predict and manage temperature rises across diverse device designs. The approach enables rapid, system-level optimization and is adaptable to various tissues and organs, providing a foundational tool for the safe and effective development of next-generation bio-optoelectronic technologies.

Explore
Early prototypes with exciting performance and new methodology

Wu et al., 2025, Device *3*, 100898
November 21, 2025
https://doi.org/10.1016/j.device.2025.100898

CellPress

Please cite this article in press as: Wu et al., Analysis and management of thermal loads generated *in vivo* by miniaturized optoelectronic implantable devices, Device (2025), https://doi.org/10.1016/j.device.2025.100898

Device

CellPress

Article

Analysis and management of thermal loads generated *in vivo* by miniaturized optoelectronic implantable devices

Mingzheng Wu,[1,19] Kaiqing Zhang,[2,3,19] Priscilla J.Y. Fok,[1,4,19] Haohui Zhang,[2,19] Andrew I. Efimov,[1,5,19] Yue Wang,[1,5] Jingyuan Feng,[1,6] Shupeng Li,[2] Jianyu Gu,[1] Xinyue Lu,[1] Dane Hintermueller,[1,8] Liangsong Zeng,[1,7] Jinglan Zhang,[9] Emily A. Waters,[5,10,11] Tianyu Yang,[1,12] Jiaqi Liu,[1] Glingna Wang,[1,13] Zengyao Lv,[2] Yuanting Wei,[2] Yiyuan Yang,[14] Chad R. Haney,[5,10,11] Yevgenia Kozorovitskiy,[9,11] Raudel Avila,[15] Abraham Vázquez-Guardado,[16,*] Yonggang Huang,[1,2,6,7,*] and John A. Rogers[1,5,6,7,17,18,20,*]

[1]Querrey Simpson Institute for Bioelectronics, Northwestern University, Evanston, IL 60208, USA
[2]Department of Civil and Environmental Engineering, Northwestern University, Evanston, IL 60208, USA
[3]State Key Laboratory of Structural Analysis, Optimization and CAE Software for Industrial Equipment, Department of Engineering Mechanics, Dalian University of Technology, Dalian, Liaoning 116024, China
[4]School of Mechanical and Aerospace Engineering, Nanyang Technological University, Singapore 639798, Singapore
[5]Department of Biomedical Engineering, Northwestern University, Evanston, IL 60208, USA
[6]Department of Materials Science and Engineering, Northwestern University, Evanston, IL 60208, USA
[7]Department of Mechanical Engineering, Northwestern University, Evanston, IL 60208, USA
[8]Neurolux Inc., Northfield, IL 60093, USA
[9]Department of Neurobiology, Northwestern University, Evanston, IL 60208, USA
[10]Center for Advanced Molecular Imaging, Northwestern University, Evanston, IL 60208, USA
[11]Chemistry of Life Processes Institute, Northwestern University, Evanston, IL 60208, USA
[12]School for Engineering of Matter, Transport and Energy, Arizona State University, Tempe, AZ 85281, USA
[13]Pritzker School of Molecular Engineering, The University of Chicago, Chicago, IL 60637, USA
[14]Department of Biomedical Engineering & N.1 Institute for Health, National University of Singapore, Singapore 117456, Singapore
[15]Department of Mechanical Engineering, Rice University, Houston, TX 77005, USA
[16]Department of Electrical and Computer Engineering, North Carolina State University, Raleigh, NC 27606, USA
[17]Center for Bio-Integrated Electronics, Northwestern University, Evanston, IL 60208, USA
[18]Department of Neurological Surgery, Feinberg School of Medicine, Northwestern University, Chicago, IL 60611, USA
[19]These authors contributed equally
[20]Lead contact
*Correspondence: abraham.vg@ncsu.edu (A.V.-G.), y-huang@northwestern.edu (Y.H.), jrogers@northwestern.edu (J.A.R.)
https://doi.org/10.1016/j.device.2025.100898

THE BIGGER PICTURE Implantable optoelectronic devices are transforming how we interface with biological systems, offering precise control and sensing capabilities with high spatial and temporal resolution. As these technologies become more miniaturized and powerful, however, managing *in vivo* thermal loads has emerged as a key challenge for both safety and performance. Even small temperature increases can alter cellular excitability, making thermal control essential. Despite growing awareness of this issue, no unified framework currently exists to predict and manage heat generation across diverse device architectures and operating conditions, hindering the ability to compare systems or optimize designs effectively.

This study introduces a generalizable framework for estimating and managing temperature rise from implantable optoelectronic systems. It proposes the Green's function to solve the coupled thermal-optical equation analytically, thereby deriving temperature distributions generated by optoelectronic sources. Numerical simulations provide scaling factors to account for the influence of non-analytical parameters, and *in vivo* characterizations validate device optimization guided by the analyses. This unified approach enables rapid, quantitative assessment of how device geometry, material properties, and emission profiles influence thermal load in brain tissue, allowing systematic device optimization to reduce local heating without compromising functionality. Importantly, the framework is scalable and modular. It supports future expansion to multi-source systems and integration with emerging active cooling technologies. Beyond neural applications, this methodology can be adapted for use in other organs (e.g., skin, muscle, and heart) where thermal management is also crucial for long-term bio-integration. By combining analytical rigor with biological relevance, this work provides the foundation for thermally informed design of next-generation bio-optoelectronic systems.

Please cite this article in press as: Wu et al., Analysis and management of thermal loads generated *in vivo* by miniaturized optoelectronic implantable devices, Device (2025), https://doi.org/10.1016/j.device.2025.100898

SUMMARY

Miniaturized implantable optoelectronic technologies for *in vivo* biomedical applications are gaining interest but require strict thermal management for safe operation. Here, we introduce a comprehensive framework combining analytical solutions and numerical modeling to estimate and manage thermal effects of optoelectronic devices. We propose Green's functions to analytically solve temperature distributions in tissue from a point source with coupled thermal-optical power, capturing the influence of critical tissue properties and spatiotemporal parameters. Integrating the Green's function derives temperature distributions for sources with definable geometries. Numerical modeling defines scaling factors to account for variations in radiation patterns and material designs, enabling direct performance comparisons across systems. Guided by this framework, iterative optimization of a filamentary optogenetic probe for deep brain stimulation significantly reduces thermal loads while preserving typical behaviors in freely moving mice. Experimental validation through *in vitro* and *in vivo* characterization demonstrates scalable strategies to overcome thermal challenges in advanced bio-optoelectronic systems.

INTRODUCTION

Emerging classes of high-performance, miniaturized optoelectronic technologies are transforming possibilities in biomedical microsystems for research and clinical applications.[1–8] Recent advances in biomaterials and device-level integration schemes serve as the basis for sub-millimeter-scale, and even cellular- and sub-cellular-scale, light sources and photodetectors to deliver and sense light in biological tissues with ultra-thin, flexible, minimally invasive, and biomimetic designs.[9–15] Such systems, optimized for compatibility with soft biological tissues, often feature conformal contacts with curvilinear surfaces to enhance performance at the biointerface. Deployment of high-power, miniature light sources on flexible substrates faces challenges, however, due to the limited heat-dissipation capacities of polymeric materials that are typically used,[16] thereby creating the potential for significant thermal stresses for *in vivo* applications. For example, implantable filamentary probes for optogenetic neural stimulation, if not properly designed, optimized, and operated, can generate non-negligible thermal loads at the optoelectronic-neural interface,[17–19] risking off-target biological effects, impaired cellular functions, and tissue damage.[20]

The heating associated with the operation of these bio-integrated optoelectronic devices primarily originates from two sources. First, the absorption of photons in biological tissues produces photothermal effects that elevate temperatures in the illuminated regions.[21] Second, the operation of light-emitting diodes (LEDs) involves non-radiative processes and Ohmic losses that contribute additional thermal loads.[22] Thus, effective thermal estimation and management are essential for designs and operating parameters that maintain biologically safe conditions *in vivo* and ensure reliable outcomes.

Studies using numerical modeling and experimental characterization, both *ex vivo* and *in vivo*, demonstrate a wide range of temperature changes that can be introduced by various light-delivering systems.[20,23–27] These results show that cellular responses to local temperature changes, such as the non-specific activation of transient receptor potential (TRP) channels[28,29] or potassium channels (e.g., K_{2P} and K_{ir})[20,30] during standard photostimulation protocols, cannot be ignored when designing experiments and interpreting data. Despite this knowledge, the absence of a unified framework to estimate thermal loads across experimental and design parameters hampers efforts to compare performance across systems and to guide engineering designs, which are essential for improving heat dissipation of *in vivo* optoelectronic systems.

This work introduces a comprehensive treatment of this problem, which combines analytical solutions, numerical modeling, and *in vivo* experimental characterization to estimate, validate, and manage the thermal loads of optoelectronic devices using the mammalian brain as an example system due to its high sensitivity to temperature fluctuations (Figure 1, schematic illustration). First, we present analytical solutions for the temperature distribution in tissues generated by coupled isotropic thermal-optical sources. The results define the effects of key parameters such as input power, optical efficiency, irradiation distance, thermal and optical properties, pulse frequency, and duty cycles. These solutions, combined with numerical modeling, identify scaling factors that modulate the thermal fields generated by optoelectronic devices, to allow direct comparisons of heat management across systems in a way that accounts for differences in radiation patterns, material designs, and geometrical configurations. Using these factors, we demonstrate informed design optimizations of filamentary optoelectronic probes that effectively reduce thermal loads in the brain through passive thermal management strategies. Finally, we experimentally validate numerical results using *in vitro* and *in vivo* models, highlighting the effectiveness of this framework to predict temperature loads from various parameters without the need for iterative simulations. This work provides a robust methodology for accurately estimating the thermal loads in tissues. The immediate utility is in identifying thermal management considerations for optimizing material and geometrical designs in the rapidly advancing field of bio-integrated optoelectronics.

RESULTS

Analytical solutions for coupled isotropic thermal-optical sources

Our framework begins with the analytical solution for the steady-state temperature rise resulting from an isolated isotropic point source that produces both light (optical power, $P_{Optical}$) and

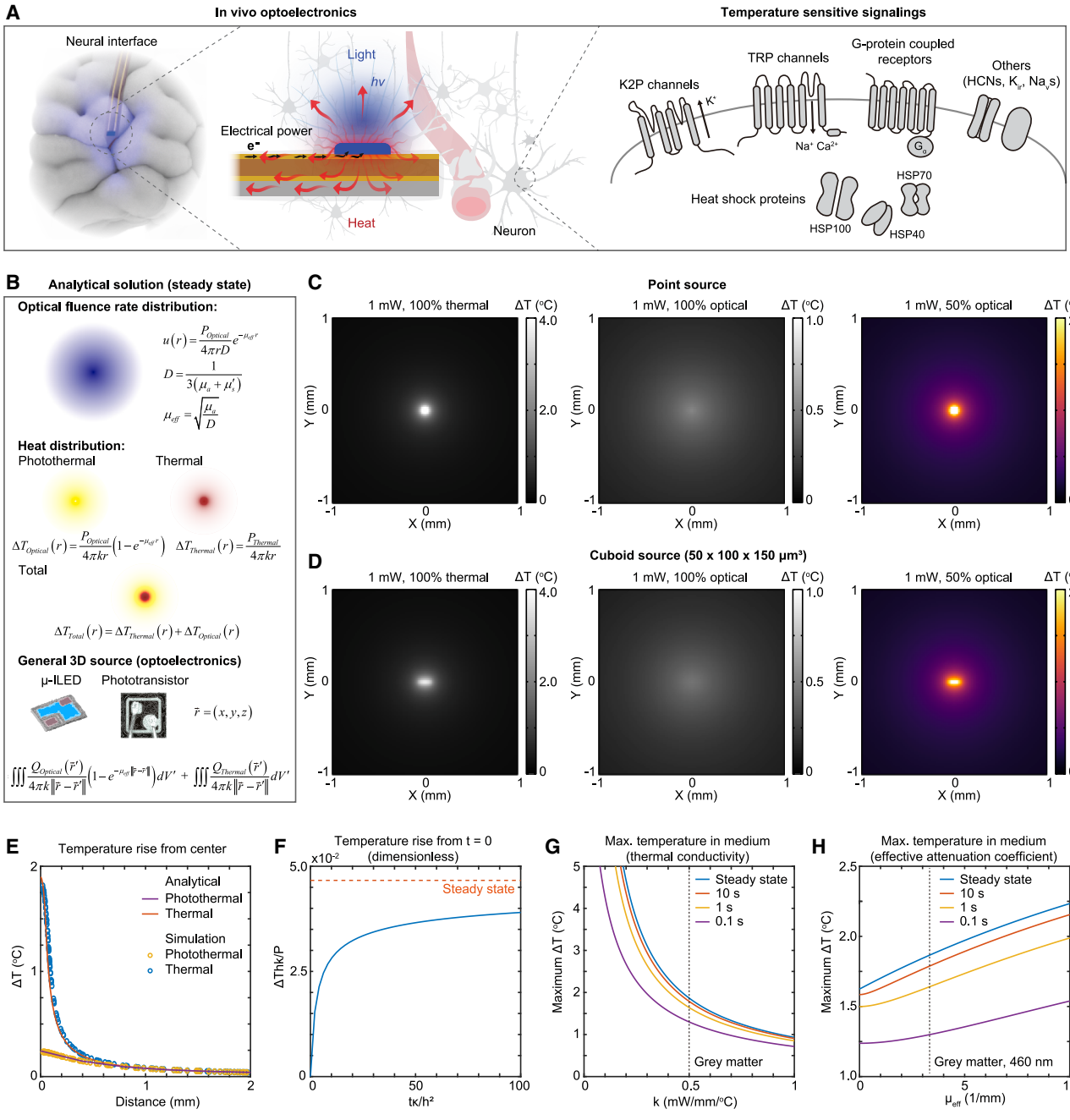

Figure 1. Analytical solution for the temperature distribution due to optical and thermal effects

(A) Unintended thermal load at the optoelectronic-tissue interface leading to changes in temperature-sensitive signalings.[20,28,30–34]

(B) Steady-state analytical solutions for the distribution of optical fluence rate, temperature distribution from optical and thermal point sources, and temperature distribution from coupled optical and thermal volumetric sources.

(C and D) Temperature contour plots showing temperature rise (ΔT) due to the optical, thermal, and their combined effect for a 1-mW total power for (C) point and (D) cuboid source.

(E) Analytical and numerical solutions that show the distance-dependent temperature (e.g., heat penetration) for a coupled thermal-optical cuboid source of 1 mW with $\alpha = 0.5$.

(F) Dimensionless temperature rise as a function of dimensionless time at 25 μm from the center of a cuboid source.

(G and H) Maximum temperature rise after 0.1, 1, 10 s and at steady-state conditions for various (G) thermal conductivities (k) and (H) effective attenuation coefficients (μ_{eff}) for a coupled thermal-optical cuboid source of 1 mW with $\alpha = 0.5$ at 25 μm from the center of a cuboid source.

See also Figure S1.

Please cite this article in press as: Wu et al., Analysis and management of thermal loads generated *in vivo* by miniaturized optoelectronic implantable devices, Device (2025), https://doi.org/10.1016/j.device.2025.100898

heat (thermal power, $P_{Thermal}$), as illustrated in Figure 1B. It assumes conduction as the dominant mode of heat transfer, within an infinite, homogeneous medium. In the analytical solution, the absorption and scattering parameters define the distribution of the optical fluence rate. The optical absorption (i.e., the optical energy lost per unit of time) at each position contributes to heat production that follows an isotropic profile throughout the medium. The thermal power produced by the source corresponds to an additional mechanism of heat production that propagates in the same isotropic profile, where the thermal properties of the material determine the propagation characteristics. Consequently, the total temperature rise (ΔT_{Total}) predicted by this model comprises two components: optically induced thermal effects ($\Delta T_{Optical}$), referred to as a photothermal source, and thermal diffusion due to Joule heating ($\Delta T_{Thermal}$), referred to as a thermal source.

Two Green's functions solve the partial differential equations (PDEs) governing photothermal and Joule heating from a point source (see method details). The first Green's function addresses the heat diffusion PDE in the medium with thermal conductivity k, based on an established solution from the literature[35]:

$$G_{Thermal}(\vec{r}, \vec{r'}) = \frac{1}{4\pi k \|\vec{r} - \vec{r'}\|}. \quad \text{(Equation 1)}$$

The second Green's function is newly proposed in this study to solve the photothermal PDE that addresses light absorption and thermal conversion in tissue:

$$G_{Optical}(\vec{r}, \vec{r'}) = \frac{1}{4\pi k \|\vec{r} - \vec{r'}\|}\left(1 - e^{-\mu_{eff}\|\vec{r}-\vec{r'}\|}\right). \quad \text{(Equation 2)}$$

Remarkably, the resulting temperature rise from photothermal heating depends solely on k and the effective optical attenuation coefficient μ_{eff}.

In the transient state, time t further defines the thermal and optical governing equations, requiring two time-dependent Green's functions to solve transient-state PDEs (see method details). For a general volumetric source, integrating the Green's function based on the geometry of the optoelectronic component provides the distribution of the optical fluence rate and the corresponding temperature rise due to the coupled three-dimensional (3D) thermal-optical power source model.

For specific temperature distributions from thermal-optical sources, analytical solutions address Joule heating and photothermal effects separately and subsequently combine them to represent the complete scenario. Here, optical efficiency refers to the ratio of total input power (P_{Total}) that is converted into optical output power ($\alpha = P_{Optical}/P_{Total}$). The medium represents typical brain tissue, with k = 0.5 mW/mm/K and μ_{eff} = 3.3 mm^{-1}.[18,36] A 1-mW point source with α = 0 produces 100% thermal power, resulting in a temperature increase of 11.30°C at the center and 1.59°C at a radial distance of 100 μm, whereas a point source with α = 1 emits 100% optical power and results in a temperature increase of 0.53°C near the center and 0.45°C at 100 μm (Figure 1C). For a cuboid source with a shape representing a typical optoelectronic component used in implantable devices for optogenetics (e.g., 50 × 100 × 150 μm^3), the maximum temperature rise at the center of the source with α = 0 and 1 is 3.79°C and 0.49°C (Figure 1D). The temperature distributions vary linearly with α for a given total power (e.g., 1 mW; Figures S1A and S1B). For example, the temperature rise at the interface for a cuboid source with α = 0.5 can be obtained by linearly interpolating between the temperature rise at the same location for the source with α = 0 and 1 (Figures 1C, 1D, S1A, and S1B). Two dimensionless functions characterize the effects of cuboid source geometry on temperature increases with different lengths, widths, and heights (Figures S1C and S1D). This finding facilitates the direct comparison of thermal effects across optoelectronic sources with varying shapes.

Finite-element analysis (FEA) validates the analytical solution for the temperature distribution due to a cuboid source operating at 1 mW with α = 0.5 at varying distances from the source center (Figure 1E). The temperature rise close to the source is largely due to Joule heating effects, which decrease sharply with distance. Conversely, photothermal effects are generally less significant close to the source but decay more slowly due to the propagation of photons into the tissue, generating additional heating throughout the medium. In addition to the spatial temperature profile from the steady-state solutions, the transient-state solution captures the relationship between temperature increase and operating time. Figure 1F shows the increase in dimensionless temperature as a function of time. As demonstrated in the Green's functions, two main factors influence the temperature distribution: the thermal conductivity (k) of the medium, which predominately regulates the temperature rise due to Joule heating effects (Figure 1G), and the effective attenuation coefficient (μ_{eff}), which primarily controls the photothermal effects (Figure 1H). The impact of other parameters, including specific heat capacity, density, scattering coefficients, and absorption coefficients, is detailed in Figures S1E–S1G.

Transient-state analytical solutions for generalized heating effects of pulsed light

Optical modulation and/or monitoring of cellular processes often requires temporally patterned illumination.[37–40] When designed effectively, this modulation can substantially reduce the increase in temperature of the tissue. Transient-state analytical solutions address temperature distributions from pulsed thermal-optical sources (see method details). Figure 2A defines the key adjustable parameters for pulsatile illumination, where the pulse frequency ($1/\tau$) defines the number of cycles within a second, and the duty cycle (DC) determines the width of the light pulses as a percentage of the total waveform period. The pulse width (DCτ) represents the duration during which the source is active. The parameter t is the total length of the modulation protocol. This pulsed-illumination operation corresponds to a pulsed thermal load in the tissue. When heat is not fully dissipated during the cooling phase of a cycle, residual heat in the medium accumulates from previous pulses, causing a progressive increase in temperature.

Integrating the Green's functions provides the spatiotemporal distribution of temperature rise from sources of any shape. Specifically, an arbitrary cuboid source (50 × 100 × 150 μm^3) operated at 1 mW, with $1/\tau$ = 5 Hz and DC = 5%, is considered for this

Please cite this article in press as: Wu et al., Analysis and management of thermal loads generated *in vivo* by miniaturized optoelectronic implantable devices, Device (2025), https://doi.org/10.1016/j.device.2025.100898

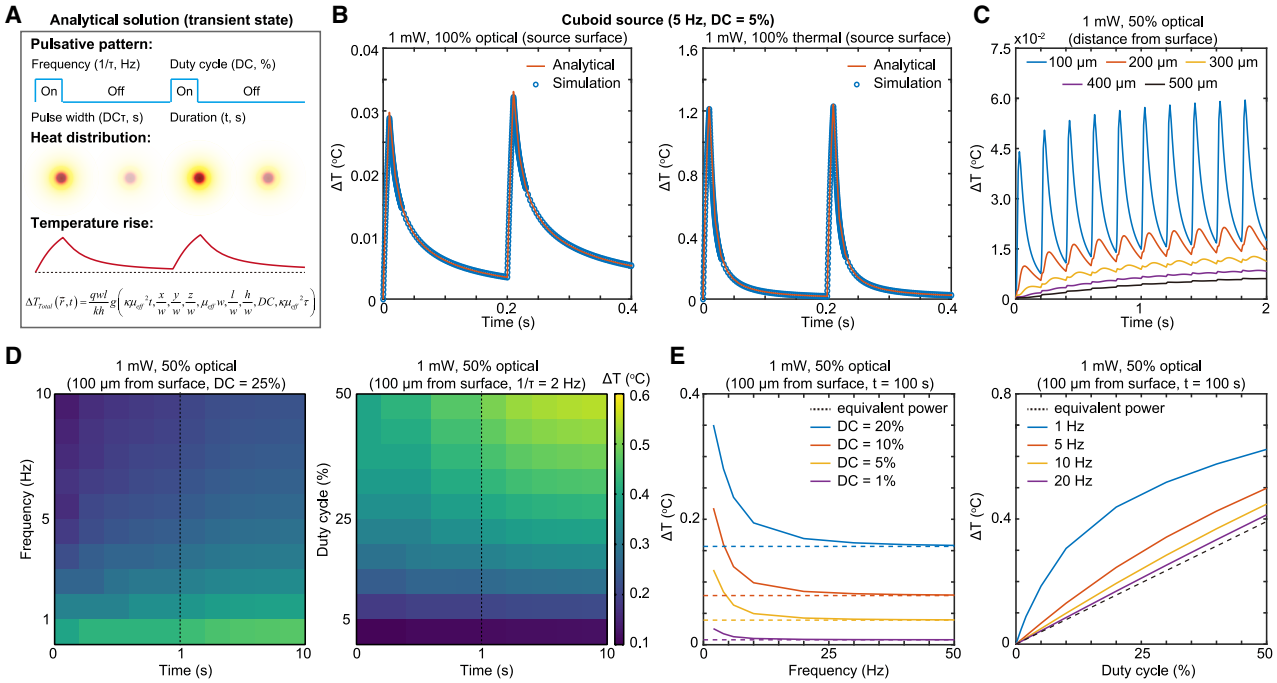

Figure 2. Transient-state temperature rise in a cuboid source operated in a pulsatile mode

(A) Transient-state analytical solution for the heat distribution and variation of temperature due to a given pulsative mode of operation.

(B) Analytical and numerical solutions for the dependence of temperature on time for an optical and thermal cuboid source, where the total power is 1 mW, pulsing frequency ($1/\tau$) is 5 Hz, and duty cycle, DC, is 5%.

(C) Temperature variation for a 1-mW cuboid source with 50% optical efficiency at different distances from the source surface (100, 200, 300, 400, and 500 μm).

(D) Heatmaps of the temperature rise (ΔT) of a 1-mW cuboid source with 50% optical efficiency at 100 μm from the surface of the source for different pulsing frequencies with DC of 5% and for different duty-cycle values with a frequency of 2 Hz.

(E) Temperature rise of a 1-mW cuboid source with 50% optical efficiency at 100 μm from the surface of the source after 100 s for different values of DC (1%, 5%, 10%, and 20%) and different $1/\tau$ (1, 5, 10, and 20 Hz).

analysis. With 100% optical power ($\alpha = 1$), the maximum temperature rise at the source-tissue surface is 0.030°C during the first cycle, which increases to 0.033°C in the second cycle. In contrast, the maximum temperature rise with 100% thermal power ($\alpha = 0$) remains constant at 1.2°C during the first two cycles (Figure 2B). Thus, photothermal effects can dominate heat accumulation under pulsatile operation. For a coupled thermal-optical source model with $\alpha = 0.5$ at a similar pulsatile profile ($1/\tau$ = 5 Hz, and DC = 5%), the pulsing nature of the light source causes substantial fluctuations in temperature near the surface of the source. However, at long distances from the source (>400 μm), the effects of pulsing diminish, and the temperature rise resembles that of a continuous source with equivalent power (Figure 2C).

The relationship between the temperature rise and the temporal parameters at 100 μm from the source surface yields additional insights (Figure 2D). As the frequency increases, the effects of the accumulation of heat decrease due to the reduction of the activation and increase of the cooling cycle times of the source. The result is a decrease in the maximum temperature rise in the surrounding tissue, approaching that of a continuous source with equivalent power at DC × 1 mW ($\alpha = 0.5$, Figure 2E). When the pulse frequency exceeds 5 Hz, the maximum temperature rise increases linearly with the duty cycle (Figure 2E). These findings suggest that increasing the frequency and decreasing the pulse width can significantly reduce the thermal load on the tissue, as might be expected.

Numerical modeling of scaling factors from anisotropic light sources

The analytical solution previously described primarily considers photothermal effects from a light source with an isotropic radiation pattern. Advanced frameworks can describe photothermal effects due to real optoelectronic components that produce anisotropic patterns of illumination. Scaling the distribution of the temperature rise for an isotropic source with 100% optical power ($\alpha = 1$) by a factor (G_r, $\Delta T/\Delta T_{Optical\text{-}Isotropic}$) reflects the photothermal effects of arbitrary anisotropic radiation patterns (Figure 3A). Three patterns of illumination are commonly encountered in experiments: a Lambertian pattern, representing typical optoelectronic light sources (e.g., LEDs); a diverging pattern, representing the emission profile of optical fibers with a given numerical aperture (NA); and a collimated pattern, representing the limited divergence nature of unidirectional lasers. For each case, Monte Carlo simulations define the spatial distribution of light in a scattering medium with optical parameters that mimic those of the target region, such as the living brain in this work (Table S1). Each source displays distinct illumination

Please cite this article in press as: Wu et al., Analysis and management of thermal loads generated *in vivo* by miniaturized optoelectronic implantable devices, Device (2025), https://doi.org/10.1016/j.device.2025.100898

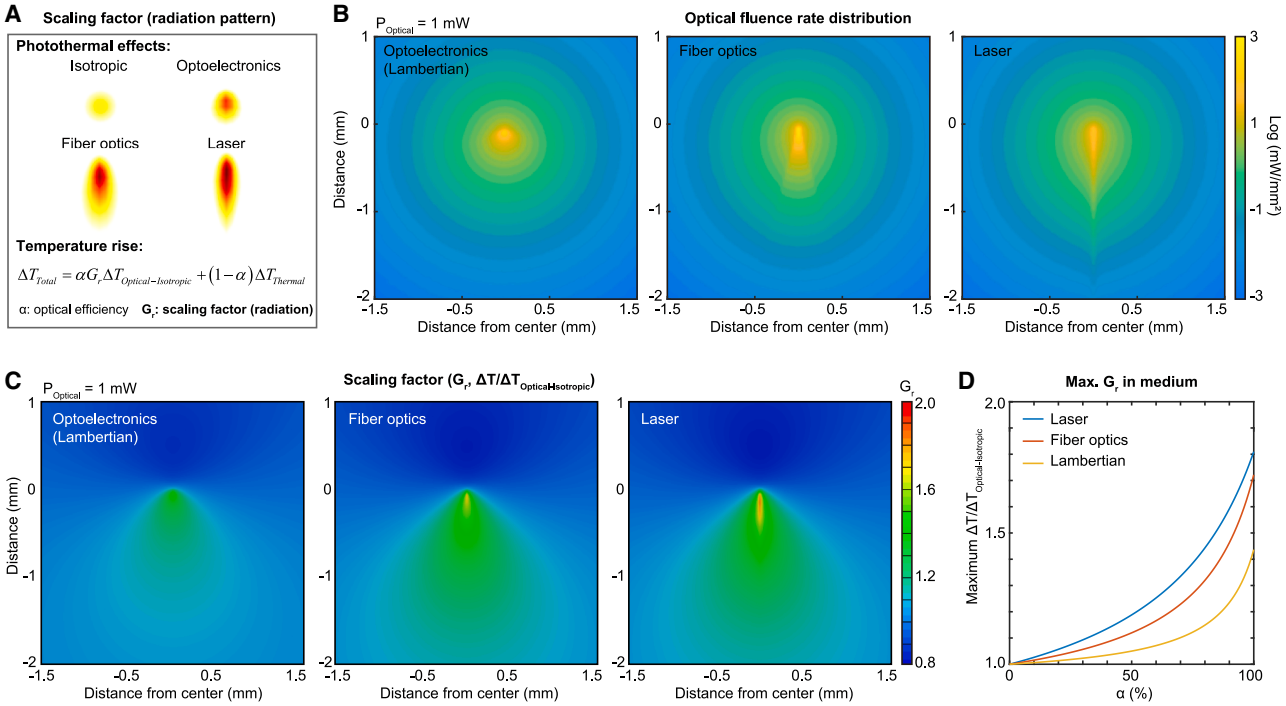

Figure 3. Comparison of scaling effects of illumination patterns for isotropic, optoelectronic, fiber optic, and laser sources

(A) Contours of illumination patterns for isotropic, optoelectronic, fiber optic, and laser sources.

(B and C) Contour plots showing the distribution of the (B) optical fluence rate and (C) scaling factor (G_r, $\Delta T/\Delta T_{Optical\text{-}isotropic}$) of a Lambertian, fiber optic, and a laser source for an optical power of 1 mW.

(D) Variation of a maximum scaling factor as a function of optical efficiency of a Lambertian, fiber optic, and laser sources.

See also Figure S2.

characteristics, as defined by its contour patterns (Figures 3B and S2A). The distribution of the optical fluence rate varies significantly depending on the source, with laser sources delivering the most concentrated irradiance under a given optical power (1 mW; Figures 3B and S2).

Contour plots of G_r for these anisotropic sources compare the photothermal effects of each relative to that of an isotropic source (Figure 3C). Although the anisotropic sources yield substantially more concentrated optical fluence compared to isotropic sources (Figure S2B), the photothermal effects remain within a factor of two of one another. Specifically, the maximum values of G_r in the field of interest for a 1-mW source with 100% optical power ($\alpha = 1$) are as follows: optoelectronics, 1.4; fiber optics, 1.7; and laser, 1.8 (at 460 nm, relative to an isotropic point source) (Figure 3D). Furthermore, these values decrease substantially as the optical efficiency of the light source declines. For optical efficiencies typical of optoelectronic components (6%–36%), the maximum value of G_r is between 1.004 and 1.03. Therefore, additional photothermal effects due to the anisotropic nature of typical optoelectronic light sources can be neglected, relative to the isotropic case.

Scaling factors from integrating materials of the light source

The use of optoelectronic components requires integration with substrates that deliver electric current and serve as a vehicle for insertion into target regions.[9–11] Encapsulation layers insulate the electrical elements from the biological environment and serve as biocompatible interfaces to minimize foreign body reactions. Modern integration strategies often feature interfaces with low Young's modulus to reduce tissue damage during natural organ movements (e.g., intracranial micromotion of the brain).[41–45] The results in Figure 1 show that an isolated source can lead to substantial increases in temperature at the tissue interface, even at relatively low power. Appropriate materials and structures for thermal management are thus important to protect the tissues from the adverse effects of heating. The use of a simplified model for the probe facilitates analysis through scaling factors due to Joule heating (thermal, $G_{p\text{-}t}$, $\Delta T/\Delta T_{Isolated}$) and photothermal ($G_{p\text{-}pt}$, $\Delta T/\Delta T_{Isolated}$) effects (Figure 4A). The model features a cuboid power source ($50 \times 100 \times 150$ μm^3) with a substrate and an encapsulation layer, each 100 μm thick and 200 μm wide.

Numerical modeling quantifies the corresponding effects of substrates with low (polyimide [PI]) or high (copper [Cu]) k, and of thermally insulating encapsulation layers (e.g., air), embedded in a biological tissue (e.g., brain tissue). The ratio of the resulting temperature distributions to those of an isolated light source with 1-mW thermal power (Figure 4B) determines $G_{p\text{-}t}$ (Figure 4C). A similar approach for a source with 1-mW optical power defines $G_{p\text{-}pt}$ for varying materials (460 nm, Lambertian pattern; Figure S3A). Comparative analysis across configurations highlights the reduction in thermal accumulation at the probe-tissue

Please cite this article in press as: Wu et al., Analysis and management of thermal loads generated *in vivo* by miniaturized optoelectronic implantable devices, Device (2025), https://doi.org/10.1016/j.device.2025.100898

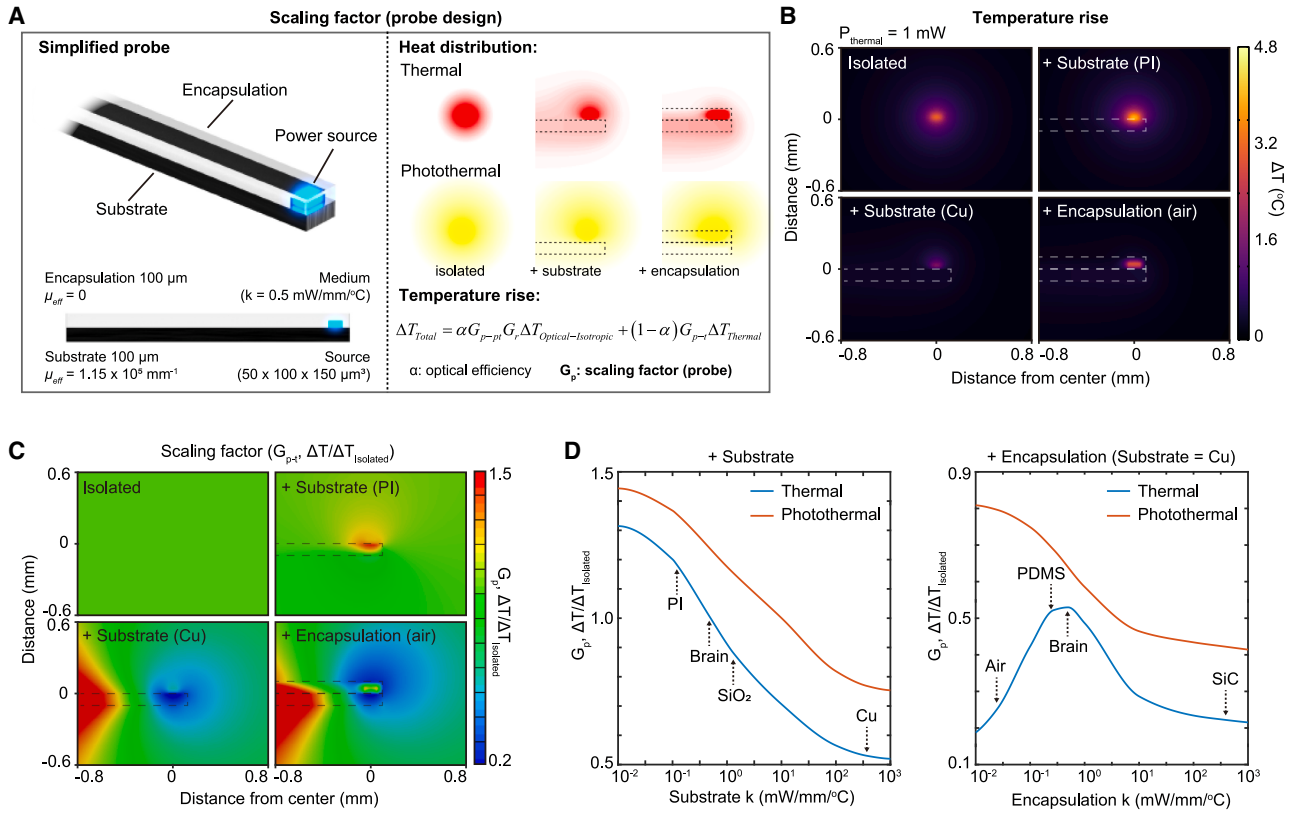

Figure 4. Scaling effects for a simplified probe design with various substrates and encapsulation materials

(A) Heat distribution and total temperature rise model that includes the scaling factor for the simplified probe design.

(B) Temperature contour plots for the temperature rise (ΔT) of the isolated source, simplified probe with PI substrate, Cu substrate, and encapsulated in air, for a thermal power of 1 mW.

(C) Contour plots of the scaling factor (G_{p-t}, $\Delta T/\Delta T_{isolated}$) for the isolated source, the simplified probe with a hypothetical PI substrate, the Cu substrate, and the air encapsulation layer in addition to Cu substrate.

(D) Variation of the scaling factors due to thermal (G_{p-t}) and photothermal (G_{p-pt}) effects at the probe-tissue interface, directly above the center of the source, as a function of the thermal conductivities (k) of the substrate and encapsulating materials (with a Cu substrate).

See also Figure S3.

interface (Figures 4C and S3A). While there is an increase in G_{p-t} and G_{p-pt} at longer distances (>0.5 mm) from the center, the absolute temperature rise in these areas is minimal and has negligible impacts on the medium.

With the simplified probe design, the results of Figure 4D summarize the influence of materials k values on G_{p-t} and G_{p-pt}, with a focus on the location at the probe-tissue interface centered above the optoelectronic source (Figure 4D). Consistent with intuition, substrate materials with high k, such as Cu, exhibit lower scaling factors and significantly reduced interface temperatures compared to those with low k due to their improved abilities to dissipate heat away from the source (Figure 4D). On the other hand, encapsulation materials with low k prevent heat from dissipating into the surrounding medium efficiently, thereby leading to low values of G_{p-t} at the probe-tissue interface. As the value of k approaches that of brain tissue, G_{p-t} increases as these insulating effects decrease. In the limit of high k, the encapsulating material creates thermal pathways that reduce heat accumulation at the probe-tissue interface, resulting in a decrease in G_{p-t}. Photothermal effects lead to a consistent trend: G_{p-pt} decreases with increasing k for the encapsulation material (Figure 4D).

Probe design optimization guided by analytical and numerical frameworks

These collective results guide the optimization of optoelectronic structures to reduce thermal loads on biological tissues. Consider, as a specific example, a probe that integrates a microscale inorganic light-emitting diode (μ-ILED) as a source, built onto a probe for *in vivo* optogenetic studies. The optimization process in this case involves iterative improvements to the materials and designs (Figure 5A). The probe consists of a flexible printed circuit board (fPCB; 75-μm-thick PI with 18-μm-thick Cu layers on both sides) as a substrate for a blue μ-ILED (TR2227, CREE; dimensions, 220 × 270 × 50 μm^3; wavelength, 460 nm) cut into a filamentary shape with a width and length of 0.50 and 6.25 mm. Narrow Cu traces (50 μm wide, separated by a 210-μm gap) serve as electrical connections between the

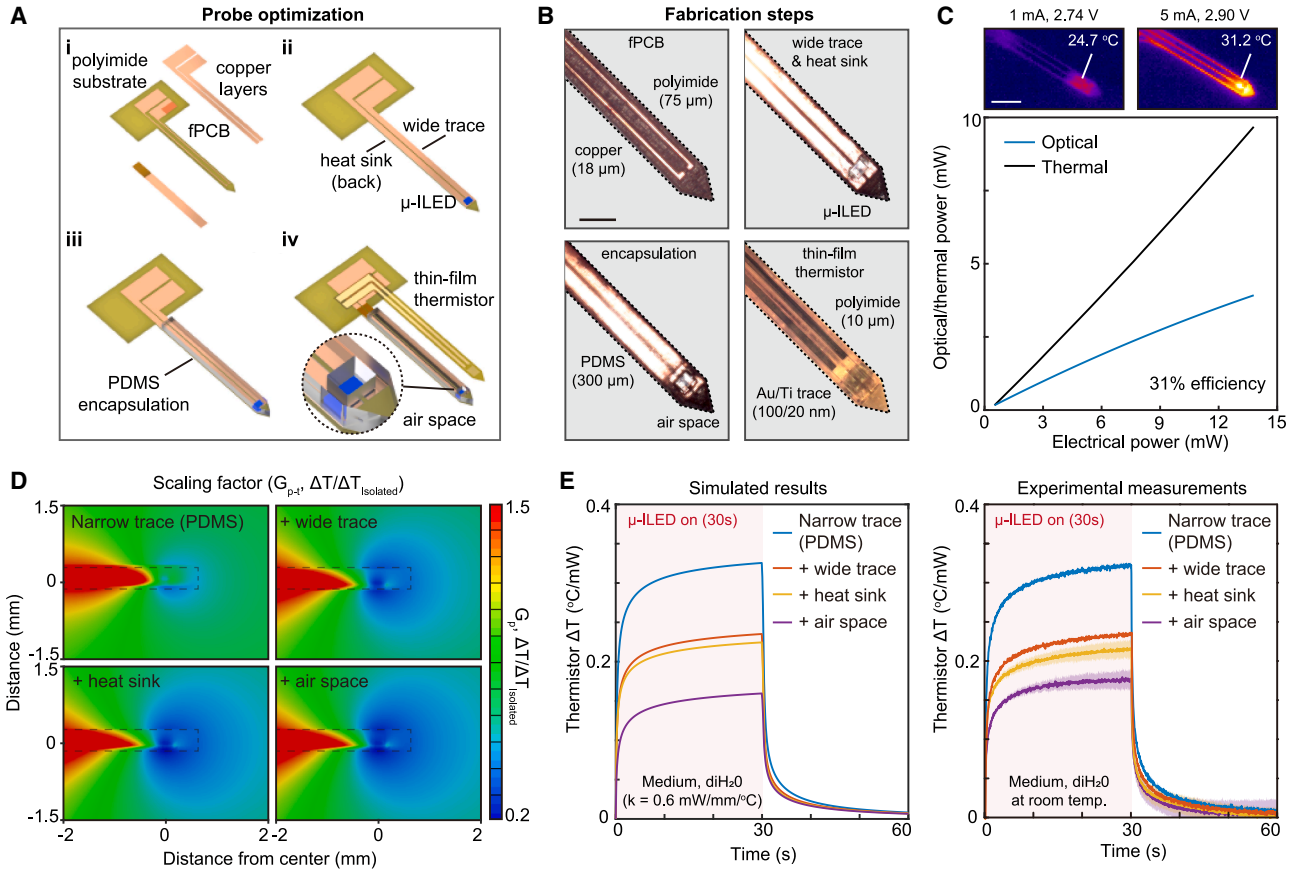

Figure 5. Probe designs and optimization processes to select features that minimize the thermal load on the surrounding medium

(A) Schematic illustrations of design features for an optoelectronic probe: (i) fPCB with Cu traces on the top and Cu heat sink on the back side of the PI substrate; (ii) optimized configuration, consisting of wide Cu traces and heat sink with μ-ILED soldered near the tip of the probe; (iii) μ-ILED encapsulated in PDMS; (iv) μ-ILED encapsulated in air with the thin-film thermistor attached on top.

(B) Optical images of probe, with examples showing narrow and wide Cu traces (thickness, 18 μm) on the PI substrate (thickness, 75 μm) with the μ-ILED soldered onto the traces. An air chamber integrated into a PDMS encapsulation structure (thickness, 300 μm) resides above the μ-ILED. The thin-film thermistor attaches on top. Scale bar, 500 μm.

(C) Thermal images of the probe activated with electrical power of 2.74 and 14.5 mW, and plot of the variation of optical and thermal power as a function of electrical power supplied to the μ-ILED. Scale bar, 1 mm.

(D) Contour plots of the scaling factor ($G_{p\text{-}t}$, $\Delta T/\Delta T_{isolated}$) for probes with narrow traces encapsulated in PDMS, wide traces encapsulated in PDMS, wide traces with heat sink encapsulated in PDMS, and wide traces with heat sink encapsulated in PDMS with an air chamber.

(E) Numerical and experimental plots of the dependence of temperature on time ($n = 5$ technical replicates) operated in water with the μ-ILED activated for 30 s. The solid lines and shaded areas represent the mean and standard deviation (SD), respectively.

See also Figure S3.

μ-ILED and an external power supply. Conventional designs also involve the removal of the Cu from the back side.

The sequential probe modification workflow produces four comparative designs. The first modification involves an increase in the width of the Cu traces (230 μm, separated by a 40-μm gap; Figure 5B). The second step is the addition of a continuous 18-μm-thick layer of Cu (0.50 × 5.5 mm^2) on the back side of the probe, which serves as an additional mechanism to dissipate heat generated by the μ-ILED. Third, encapsulation of the μ-ILED in a 300-μm-thick layer of polydimethylsiloxane (PDMS) defines an insulation barrier between the μ-ILED and the surrounding tissue. The fourth modification involves an air chamber (260 × 310 × 300 $μm^3$) to enclose the μ-ILED within the PDMS to further reduce heat transfer to the surrounding tissue. Each case involves a thin-film thermistor (10 μm) attached to the probe to monitor the temperature above the μ-ILED. The numerical model includes the geometry and material properties of this sensor (Figure 5B). Thermal imaging of the probes during operation in air reveals the Joule heating effects. Optoelectronic characterizations indicate that the optical efficiency of the μ-ILED is 31%, such that the remaining 69% contributes to Joule heating (Figure 5C).

Numerical modeling produces comparative contour plots of $G_{p\text{-}t}$ (Figure 5D) and $G_{p\text{-}pt}$ (Figure S3B) for these cases. The results demonstrate various decreases in thermal load associated with these design modifications (Figures 5D and S3B). The

Please cite this article in press as: Wu et al., Analysis and management of thermal loads generated *in vivo* by miniaturized optoelectronic implantable devices, Device (2025), https://doi.org/10.1016/j.device.2025.100898

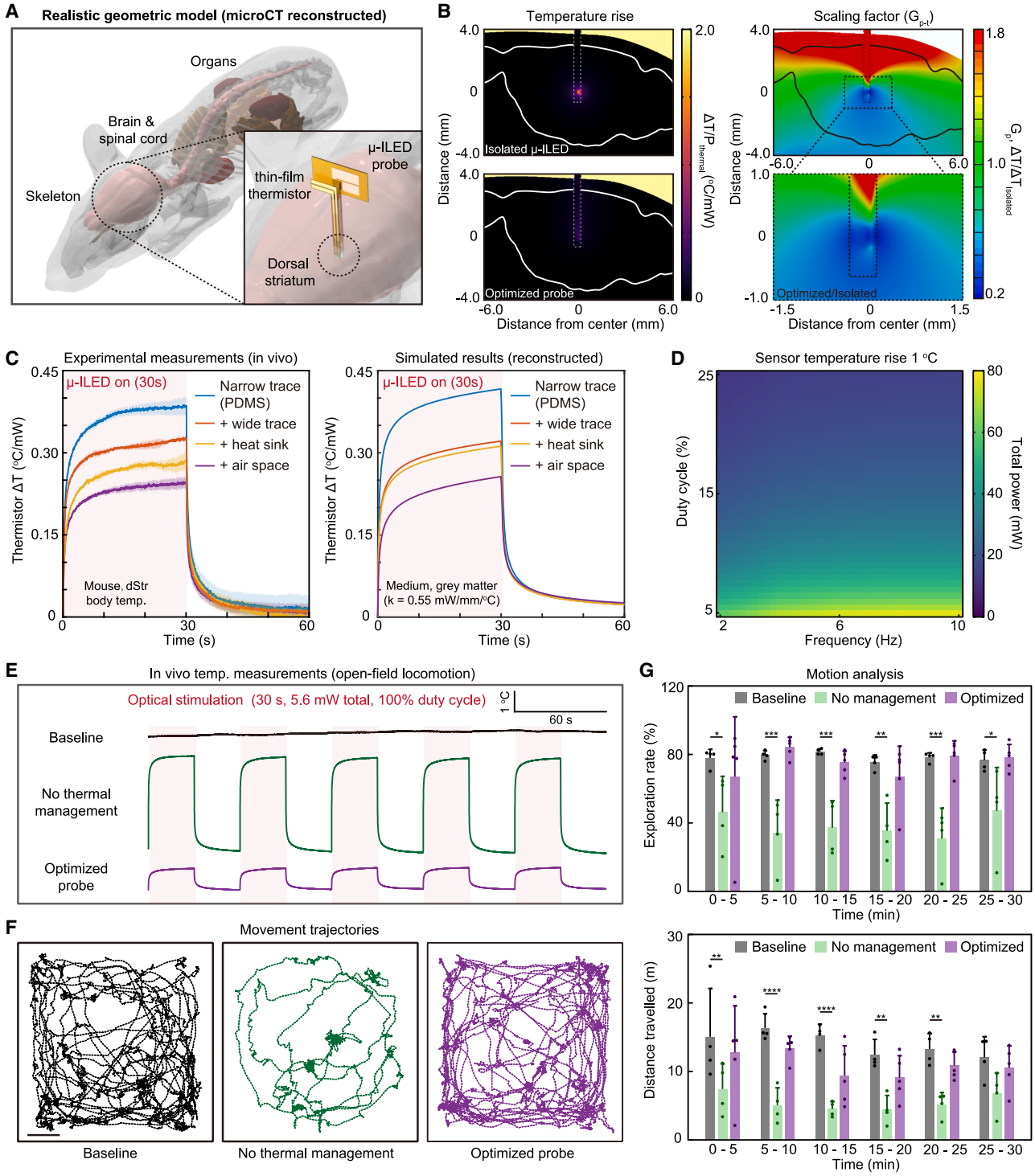

Figure 6. Numerical and experimental analysis of probe thermal performance in a realistic reconstructed model and in the living brain

(A) Geometric model rendering of a mouse using microCT reconstruction showing the probe location in the brain.

(B) Temperature contours of an isolated μ-ILED and the optimized probe design, and contour plots of the scaling factor ($G_{p\text{-}t}$, $\Delta T/\Delta T_{isolated}$) for the optimized probe in the brain.

(C) Experimental (mean ± SD, n = 5 technical replicates) and numerical temperature-time plots of the designs *in vivo* and reconstructed, respectively, with the μ-ILED on for 30 s. The solid lines and shaded areas represent the mean and SD, respectively.

(legend continued on next page)

Please cite this article in press as: Wu et al., Analysis and management of thermal loads generated *in vivo* by miniaturized optoelectronic implantable devices, Device (2025), https://doi.org/10.1016/j.device.2025.100898

optimized probe design features wide Cu traces, a heat sink (i.e., back-side Cu), and an air chamber and exhibits the lowest $G_{p\text{-}t}$ and $G_{p\text{-}pt}$ values at the probe-tissue interface. Experimental measurements with the thin-film thermistor and the blue μ-ILED operating constantly for 30 s over five continuous heating cycles (30-s heating and 30-s cooling) quantify the role of the heat sink and wide Cu traces for PDMS encapsulated probes in air, water, and ethanol (Figures 5E and S3C). Two separately fabricated probes produce similar results (Figure S3D). Additional studies examine the effect of air chambers. Experimental measurements and numerical modeling results confirm the effectiveness of the optimized design in water (0.6 mW/mm/K at room temperature; Figure 5E). Notably, the wide traces and air chamber have a more significant heat-dissipation effect than the heat sink. Related results for operation in air and ethanol yield similar trends (Figure S3E). Monte Carlo simulations demonstrate optical fluence characteristics after integrating the air chamber (Figure S3F, in water medium). While the air chamber introduces a slight refractive-index mismatch that modulates the emission profile, its low μ_{eff} preserves the overall light-delivery efficiency.

Experimental validation of probe thermal performance in the living brain

Complete analysis in the context of a specific application area focuses on probes of these types implanted into the mouse brain such as in the case of optogenetic stimulation. The geometric factors follow from the reconstruction of a 3D geometric model of a C57BL/6J mouse brain using micro-computed tomography (microCT) imaging of the cranial structure (Figure 6A). The optimized optoelectronic probe targets the dorsal striatum region. Contour plots of the resulting temperature distributions reveal a significant reduction in heating within the brain tissue when using a probe with the optimized design compared to an isolated μ-ILED (Figure 6B). Consistent with the distance-dependent temperature variations predicted in Figure 2C, the encapsulation layer reduced the peak temperature at the tissue interface by creating a 250-μm separation between the μ-ILED and the tissue interface (300-μm encapsulation and 50-μm μ-ILED height).

Temperature-time profiles captured via the thin-film thermistor during *in vivo* experiments provide additional data for comparing the four probe configurations (Figure 6C). With the μ-ILED active for 30 s, the optimized design consistently results in the lowest temperature increases. Combining experimental measurements and computed scaling factors yields a value for the k of the brain tissue (gray matter in the dorsal striatum) of ∼0.55 mW/mm/K, consistent with values reported in the literature.[46,47] The numerical model reconstructed from microCT imaging using this value of k yields simulated temperature profiles for the four probe designs with excellent correspondence to experimental results.

Integrating the scaling factors from the *in vivo* realistic geometric model with the analytical solution for the μ-ILED light source produces a heatmap that identifies the total μ-ILED power and operational parameters that maintain a temperature rise of 1°C (Figure 6D). This analysis predicts that a total power of 80 mW (∼25-mW optical power of 460-nm blue light, ∼421 mW/mm^2 at the μ-ILED) can safely operate with a 10-Hz frequency and a 5-ms pulse width as representative parameters in optogenetic protocols. Figure S4A simulates the temperature rise from the optimized optoelectronic probe in the rat brain (∼1,800 mm^3), which yields similar results compared to the mouse brain (∼400 mm^3). Further analysis reveals that the effects of increasing tissue size on the resulting temperature rise can be neglected when tissue volume is larger than 512 mm^3 (Figure S4B). These findings demonstrate the importance of proper integration strategies to regulate the thermal burden of optoelectronics in living tissue while providing critical guidance on suitable parameter ranges (e.g., power, duty cycle, frequency) for *in vivo* characterization of optoelectronic technologies and biological experiments.

Finally, to emphasize the importance of temperature management in brain tissue, we assess heat-induced off-target behavioral effects in freely moving wild-type mice. We compare the optimized probe design to a standard probe without thermal-management features (narrow-trace fPCB without a heat sink or encapsulation layer). Figure 6E illustrates temperature changes in the brain under three conditions: baseline (no power load), optical stimulation using the standard probe, and the optimized probe. Each session lasts for 30 min, with four or five replicates, and optical stimulation involves a total power load of 5.6 mW at 100% duty cycle in 30-s heating (μ-ILED on) and 30-s cooling (μ-ILED off) phases. The optimized probe maintains a maximum temperature rise of ∼1°C at the probe-tissue interface, while the probe without thermal management results in substantially higher temperature rises (Figure 6E). Behavioral assessments, including open-field tests measuring movement trajectories, exploration rates, and distance traveled over 30 min, confirm that the optimized probe minimizes thermal stress and allows mice to maintain standard activity patterns during optical stimulation at high duty cycle or pulses at high input power (5.6-mW total power, 100% duty cycle; Figures 6F and 6G; 93.2-mW total power, 20 Hz, 2-ms pulse width; Figures S5A–S5C). These results highlight the critical importance of effective thermal management in preserving physiological and behavioral integrity during *in vivo* experiments.

(D) Heatmap of the total μ-ILED power for different duty cycles and frequencies to achieve a 1°C temperature rise at the probe-tissue interface predicted by the scaling factors and analytical solutions.

(E–G) Thermal and motion analysis of freely behaving mice under baseline conditions, subjected to optical stimulation without thermal management and with the optimized probe, namely (E) *in vivo* temperature measurements, (F) movement trajectories (scale bar, 5 cm), and (G) summary data of exploration rate and distance traveled over 30 min (mean ± SD, $n = 4$ biological replicates). Two-way ANOVA, Sidak's multiple comparison with baseline, $^{*}p < 0.05$, $^{**}p < 0.01$, $^{***}p < 0.001$, $^{****}p < 0.0001$. Each dot represents a biological replicate and the error bars represent the SD. Total power load of 5.6 mW was supplied at 100% duty cycle in 30-s heating and 30-s cooling phases.

See also Figures S4–S6.

DISCUSSION

The collection of analytical solutions, numerical modeling, design optimization guidance, and *in vivo* experimental characterization results presented here establishes a comprehensive framework to address the thermal constraints of optoelectronic devices in living tissues that are susceptible to temperature perturbations. Our analytical solutions define general rules for evaluating the temperature increases generated by optoelectronic sources. The results enable the assessment of various parameters that affect the local thermal field under experimental conditions in both steady and transient states. Scaling factors derived from numerical modeling account for differences in radiation patterns, material designs, and geometrical configurations, facilitating comparisons of heat-management capabilities across systems. Combined with the analytical solutions described here, we present an efficient scheme for estimating brain thermal load under diverse experimental parameters, eliminating the need for time-consuming iterations of simulation work. By addressing the thermal challenges inherent in optoelectronic applications, this methodology supports the development of more reliable and physiologically compatible technologies for neuroscience and biomedical applications.

An integrated strategy for thermal analysis in implantable optoelectronics

Our study provides fundamental insights into optically induced thermal effects and thermal diffusion due to Joule heating of optoelectronic sources. The findings form the basis for calculating temperature loads per unit of power input into the system. In simplified scenarios, such as an isolated optical or thermal source (e.g., microscopy in living tissue) positioned in a medium with well-established optical and thermal parameters (e.g., brain tissue), these analytical solutions can readily estimate the temperature distribution in 3D space. Furthermore, the results facilitate comparisons of the temperature increase due to fully optical, thermal, or coupled sources, providing a reliable foundation for predicting the thermal performance of different optoelectronic devices. Integrating the Green's function over device geometry accounts for the effects of varying source shapes. The effective attenuation coefficient (μ_{eff}) captures the combined absorption and scattering effects of photons in biological tissue, allowing our framework to model sources with different emission wavelengths. The optical efficiency parameter (α) represents the net fraction of electrical power converted into light, reflecting the cumulative effects of quantum efficiency, light extraction, and packaging losses.

Given the physical principles of heat diffusion in biological tissue, the temperature field in a given system must adhere to the general rules of heat distribution as described in the analytical solution, for example, dictated by the thermal conduction PDE. In many cases, however, a purely analytical solution cannot accurately represent the distributions of temperature in practical applications.[18,48–50] Detailed parameters, such as radiation patterns, multilayer geometric designs of optoelectronic components, and anatomical features of the targeted tissues, can significantly alter the resulting heat-generation and transport characteristics. Variations in these factors, along with differences in power load and temporal dynamics, can frustrate comparisons of the thermal-management capabilities of different systems. A scaling framework that isolates the effects of these non-analytical parameters avoids this limitation. This approach illustrates how physical, engineering, and biological considerations modulate the thermal field when considered in conjunction with our analytical solutions. Using the obtained scaling factors, commonly used optoelectronic designs can be analyzed to understand thermal-management capabilities more effectively and to identify key parameters for targeted optimizations.

Table S3 summarizes the thermal effects of the parameters examined in this work. Beyond these analytical and non-analytical parameters, several additional factors may influence the scaling outcomes. For example, the thicknesses of the encapsulation and substrate layers can vary widely depending on fabrication method and device architecture. Thicker encapsulation layers increase thermal resistance and reduce peak surface temperatures, while thinner layers allow more rapid heat dissipation through the tissue and increase the risk of localized hot spots. Other variables, such as contact surface area and material anisotropy, can also significantly affect thermal distribution. The scaling factor framework is modular and extensible to incorporate additional parameters, ensuring broad applicability for future thermal analyses of complex bio-integrated optoelectronic systems.

Optimizing passive thermal management in implantable optoelectronics

Focused studies involve a simplified probe design with substrate and encapsulation layers typically present in optoelectronic devices and their effects on the temperature rise at the probe-tissue interface. The integration of substrate materials with high k can facilitate dissipation of heat generated by the source, while modifications to the encapsulation layer can either retain heat within the probe structure or aid in its transport along the probe. Guided by these principles, we select four comparative designs to represent progressive modifications to optimize thermal performance in flexible neural interfaces. These configurations reflect practical device geometries and widely accessible material choices (e.g., fPCB),[12,18,19,49,51,52] ensuring the relevance of our modeling framework for real-world applications.

Our optimized design incorporates an air chamber within the encapsulation to provide further thermal insulation due to the significantly lower thermal conductivity of air (~0.026 W/m·K). Consequently, it forces heat to dissipate preferentially through the substrate, thereby lowering peak interface temperatures compared to a solid PDMS encapsulation layer. One drawback, however, of the use of a substrate with high k and an encapsulation layer with low k is that heat may preferentially dissipate into surrounding tissue through the substrate. Thus, the configuration may be further improved by modifying 2D layers into a 3D structure that completely surrounds the inner substrate of high k with a low k material, such as in a cylindrical probe design (Figure S6). Such an insulation barrier increases the thermal resistance in all directions around the source so that heat

Please cite this article in press as: Wu et al., Analysis and management of thermal loads generated *in vivo* by miniaturized optoelectronic implantable devices, Device (2025), https://doi.org/10.1016/j.device.2025.100898

dissipates mainly through the inner substrate core, thus reducing the thermal load on surrounding tissue.

Another important consideration is mechanical compliance. PI-based systems are favored due to their flexibility to conform to soft-tissue surfaces and robustness for surgical handling and implantation. While widening Cu traces on PI substrates can lead to an increase in stiffness, this effect is minimal in systems employing ultra-thin films, where mechanical flexibility is primarily dictated by the substrate rather than the trace geometry.[42] In such systems, widening metal traces can still significantly enhance lateral heat dissipation without substantially compromising mechanical compliance. Future designs may benefit from the integration of advanced low-modulus and ultra-low-k materials (e.g., aerogels),[53,54] which offer mechanical properties matching native tissue with enhanced heat management.

Biological considerations in this framework

The brain is one of the most temperature-sensitive organs in the body, with tightly regulated homeostatic mechanisms that maintain thermal stability.[55–57] Physiological brain temperature can fluctuate by up to ~2°C during naturalistic behaviors.[55] For chronic applications, a more conservative safety limit of 1°C is commonly adopted to mitigate the risk of sustained thermal stress, glial activation, or unintended neuromodulation.[20,58–60] In our *in vivo* characterizations, the maximum temperature rise (ΔT) observed at the optimized probe-tissue interface was approximately 0.9°C, resulting in a short-term temperature shift below 39°C. These values fall within the range of normal physiological fluctuations and remain below thresholds associated with histological damage or behavioral disruption in rodent models.[20,23,61,62]

Although a 1°C–2°C increase is generally considered biologically safe, sub-degree temperature changes may modulate neural excitability through the activation of thermosensitive ion channels and signaling cascades (Figure 1A). Members of the TRP family (e.g., TRPV1–4) and certain potassium channels (e.g., TRAAK) are intrinsically responsive to thermal fluctuations.[63–65] The thermal sensitivity of these pathways highlights the importance of minimizing even sub-degree temperature increases to avoid unintended modulation of neural activity. In addition, the optical readouts of many genetically encoded fluorescent sensors commonly used in neuroscience are temperature sensitive.[66] These considerations reinforce the value of accurate thermal characterization and highlight the need for appropriate control experiments in optically based neuromodulation or imaging studies.

Our analytical approach assumes an infinite, homogeneous, and isotropic medium. This approximation is appropriate when the heat source is small relative to the surrounding tissue volume and sufficiently distant from anatomical boundaries—conditions generally satisfied by our implanted probes in the mouse brain (Figures 6B and S4C). While this assumption is supported by the strong agreement with numerical modeling, deviations may arise near structural interfaces, such as gray-white matter boundaries and vascular structures, where local variations in tissue-specific properties (e.g., k and μ_{eff}) could affect temperature distributions. To address these limitations, we complement our analytical model with anatomically realistic numerical simulations, based on a microCT-reconstructed mouse brain. Future studies may adapt this combined approach for thermal estimation in heterogeneous biological systems, particularly in systems requiring high spatial precision near sensitive anatomical interfaces.

Beyond structural heterogeneity, additional physiological heat-transport mechanisms such as blood perfusion and cerebrospinal fluid (CSF) convection can also influence local brain temperatures. These convection factors are often approximated using models like the Pennes' bioheat equation.[67] In our case, omitting these mechanisms did not substantially impact agreement with experimental measurements, suggesting that conduction remains the dominant mode of heat transfer under the spatial and temporal scales considered in this study. Nevertheless, modeling blood perfusion and CSF flow may be necessary for applications involving larger devices, longer heating durations, or regions with particularly high vascularization.

Future directions

This study presents, to our knowledge, the Green's function for the coupled thermal-optical problem for the first time. Based on the Green's function, we develop a series of analytical solutions for calculating the temperature rise induced by coupled thermal-optical sources. In addition, we introduce a unified methodology that integrates analytical solutions, numerical simulations, and experimental validations to evaluate and manage thermal constraints in implantable optoelectronic devices. Future advances in implantable optoelectronic systems may demand increasingly sophisticated device architectures, such as arrays of emitters, integrated active cooling elements, and complex multilayer designs. Our framework can accommodate these additional considerations. For example, both the analytical and numerical approaches are extendable to multi-source configurations. The analytical solution supports linear superposition based on Green's functions, allowing the total temperature rise from multiple sources to be calculated as the sum of their individual contributions (Figure S6C). Similarly, the numerical simulations can be adapted to incorporate multiple emitters with varied power levels, spatial distributions, and emission profiles.

Future modification of this approach may guide other heat-management strategies (e.g., microfluidic or thermoelectric cooling) by incorporating additional convective heat transfer terms or specifying heat-removal boundary conditions.[68–70] For example, microfluidic cooling channels can be represented as independent convective pathways that enable targeted heat removal in high-power or temperature-sensitive applications. These capabilities broaden the applicability of our framework to a wide range of emerging bio-integrated platforms.

Finally, the results introduced here can successfully guide probe optimization within anatomically realistic geometric constraints digitally reconstructed from mouse cranial structures. Emerging advances, such as digital twins in personalized medicine, provide increasingly detailed anatomical datasets that this approach can leverage to design individualized optoelectronic

Please cite this article in press as: Wu et al., Analysis and management of thermal loads generated *in vivo* by miniaturized optoelectronic implantable devices, Device (2025), https://doi.org/10.1016/j.device.2025.100898

probes with enhanced thermal performance.[71–73] While our experimental designs focus on neural tissue, our framework can easily adapt to other organ systems, such as the heart, muscle, and skin, by modifying tissue-specific thermal and optical parameters (e.g., k and μ_{eff}). Collectively, our findings and solutions offer an adaptable strategy for the thermal management of next-generation bio-integrated optoelectronics for safe and effective operation across a wide range of biomedical applications.

METHODS

Experimental model and subject details

Mouse

All animal-handling protocols were approved by the Northwestern University Animal Care and Use Committee. This study used adult male and female mice (aged 80–120 days, weighing 20–30 g at the start of experiments). Prior to experimentation, the mice were group-housed under standard conditions, maintained at an ambient temperature of approximately 25°C, with a 12-h light/dark cycle (lights on at 6:00 or 7:00). Enrichment included plastic igloo shelters and nesting materials. Mice from the same litter were randomly assigned to different experimental groups. We used C57BL/6 mice obtained from Charles River (Wilmington, MA) and bred in-house. All mice used in this study were healthy, immunocompetent, and had no previous experimental history.

Method details

Steady-state solution

At steady state, the 3D thermal-optical coupled equation comprises the thermal component, which addresses heat conduction within an infinite medium, and the optical component, which calculates the light propagation within the material and solves for the optical fluence rate $u(\vec{r})$ using heat source $Q_{Thermal}(\vec{r})$ and optical source $Q_{Optical}(\vec{r})$, defined by spatial position vector $(\vec{r})$:

$$Thermal\begin{cases} -k\nabla^2 T(\vec{r}) = \mu_a u(\vec{r}) + Q_{Thermal}(\vec{r}) \\ \lim\limits_{\|\Omega\|\to+\infty} T(\vec{r}) = 0 \end{cases}$$

$$Optical\begin{cases} -D\nabla^2 u(\vec{r}) + \mu_a u(\vec{r}) = Q_{Optical}(\vec{r}) \\ \lim\limits_{\|\Omega\|\to+\infty} u(\vec{r}) = 0 \end{cases}$$

Key parameters include thermal conductivity k, the reduced scattering coefficient μ_s', the absorption coefficient μ_a, and the diffusion coefficient D:

$$D = \frac{1}{3(\mu_a+\mu_s')}$$

The Green's function method

To solve this problem, we apply the Green's function based on the principle of linear superposition. Using this method, the thermal-optical coupled equation is divided into two parts and the total temperature rise is obtained by adding the contributions from both thermal and optical sources:

$$Thermal\begin{cases} -k\nabla^2 T_{Thermal}(\vec{r}) = Q_{Thermal}(\vec{r}) \\ \lim\limits_{\|\Omega\|\to+\infty} T_{Thermal}(\vec{r}) = 0 \end{cases}$$

$$Optical\begin{cases} -k\nabla^2 T_{Optical}(\vec{r}) = \mu_a u(\vec{r}) \\ -D\nabla^2 u(\vec{r}) + \mu_a u(\vec{r}) = Q_{Optical}(\vec{r},\vec{r}') \\ \lim\limits_{\|\Omega\|\to+\infty} T_{Optical}(\vec{r}) = 0 \\ \lim\limits_{\|\Omega\|\to+\infty} u(\vec{r}) = 0 \end{cases}$$

$$T_{Total}(\vec{r}) = T_{Thermal}(\vec{r}) + T_{Optical}(\vec{r})$$

The following equations represent the solution for the Green's function of the thermal component:

$$-k\nabla^2 G_{Thermal}(\vec{r},\vec{r}') = \delta(\vec{r},\vec{r}') \lim_{\|\Omega\|\to+\infty} G_{Thermal}(\vec{r},\vec{r}') = 0$$

$$G_{Thermal}(\vec{r},\vec{r}') = \frac{1}{4\pi k\|\vec{r}-\vec{r}'\|}$$

For optically induced thermal effects, the Green's function can be derived by solving the governing equation in two steps:

$$\begin{cases} -k\nabla^2 G_{Optical}(\vec{r},\vec{r}') = \mu_a u(\vec{r},\vec{r}') \\ -D\nabla^2 u(\vec{r},\vec{r}') + \mu_a u(\vec{r},\vec{r}') = \delta(\vec{r},\vec{r}') \\ \lim\limits_{\|\Omega\|\to+\infty} G_{Optical}(\vec{r},\vec{r}') = 0 \\ \lim\limits_{\|\Omega\|\to+\infty} u(\vec{r},\vec{r}') = 0 \end{cases}$$

First, we solve for the Green's function related to the 3D optical propagation:

$$-D\nabla^2 u(\vec{r},\vec{r}') + \mu_a u(\vec{r},\vec{r}') = \delta(\vec{r},\vec{r}') \lim_{\|\Omega\|\to+\infty} u(\vec{r},\vec{r}') = 0$$

$$G_{OFR}(\vec{r},\vec{r}') = \frac{1}{4\pi D\|\vec{r}-\vec{r}'\|} e^{-\mu_{eff}\|\vec{r}-\vec{r}'\|}$$

This is governed by the effective attenuation coefficient μ_{eff}, which influences how light is scattered and absorbed within the medium:

$$\mu_{eff} = \sqrt{\frac{\mu_a}{D}}$$

The second step solves the temperature rise due to heat conduction:

$$-k\nabla^2 G_{Optical}(\vec{r},\vec{r}') = \mu_a u(\vec{r},\vec{r}') \lim_{\|\Omega\|\to+\infty} G_{Optical}(\vec{r},\vec{r}') = 0$$

Please cite this article in press as: Wu et al., Analysis and management of thermal loads generated *in vivo* by miniaturized optoelectronic implantable devices, Device (2025), https://doi.org/10.1016/j.device.2025.100898

Using the Green's function method, we calculate the temperature rise generated by the photothermal interaction:

$$G_{Optical}(\vec{r},\vec{r'}) = \int_{\Omega} \mu_a u(\vec{r},\vec{r'}) G_{Thermal}(\vec{r},\vec{r'}) d\Omega'$$

Solving the above integral gives us the Green's function for the photothermal PDE:

$$G_{Optical}(\vec{r},\vec{r'}) = \frac{1}{4\pi k\|\vec{r}-\vec{r'}\|}\left(1-e^{-\mu_{eff}\|\vec{r}-\vec{r'}\|}\right)$$

Interestingly, the resulting temperature increase depends only on μ_{eff} and is independent of other optical parameters.

For a general source, the solutions for both the optical fluence rate distribution and the temperature rise can be obtained by integrating the Green's function over the source's geometry.

The optical fluence rate distribution for a general source is defined as:

$$u(\vec{r}) = \int_{\Omega} Q_{Optical}(\vec{r'}) G_{OFR}(\vec{r},\vec{r'}) d\Omega'$$

The distribution of the temperature rise for a general source is given by:

$$T_{Optical}(\vec{r}) = \int_{\Omega} G_{Optical}(\vec{r},\vec{r'}) Q_{Optical}(\vec{r'}) d\Omega'$$

$$T_{Thermal}(\vec{r}) = \int_{\Omega} G_{Thermal}(\vec{r},\vec{r'}) Q_{Thermal}(\vec{r'}) d\Omega'$$

$$T_{Total}(\vec{r}) = T_{Optical}(\vec{r}) + T_{Thermal}(\vec{r})$$

For a point source, the following equations are used to determine the optical fluence rate distribution:

$$Q_{Optical}(\vec{r'}) = P_{Optical}\delta\left(\vec{r'},\vec{0}\right)$$

$$u(r) = \frac{P_{Optical}}{4\pi D r} e^{-\mu_{eff} r}$$

The resulting distribution of the temperature rise for a point source can be calculated directly at different spatial locations:

$$T_{Optical}(r) = \frac{P_{Optical}}{4\pi k r}\left(1-e^{-\mu_{eff} r}\right)$$

$$T_{Thermal}(r) = \frac{P_{Thermal}}{4\pi k r}$$

$$T_{Total}(r) = T_{Thermal}(r) + T_{Optical}(r)$$

Transient-state solution

In the transient-state problem, the 3D thermal-optical coupled equations are further defined by time (t). Key parameters include specific heat c and the material density ρ. The thermal component is governed by the transient thermal conduction PDE:

$$\begin{cases} c\rho \dfrac{\partial T_{Thermal}(\vec{r},t)}{\partial t} - k\nabla^2 T_{Thermal}(\vec{r},t) = Q_{Thermal}(\vec{r},t) \\ \lim\limits_{\|\Omega\|\to+\infty} T_{Thermal}(\vec{r},t) = 0 \\ T_{Thermal}(\vec{r},t)|_{t=0} = 0 \end{cases}$$

The photothermal component accounts for the heat generated from optical absorption, which is calculated using the transient thermal-optical coupled PDE:

$$\begin{cases} c\rho \dfrac{\partial T(\vec{r},t)}{\partial t} - k\nabla^2 T(\vec{r},t) = \mu_a u(\vec{r},t) \\ \mu_a u(\vec{r},t) - D\nabla^2 u(\vec{r},t) = Q_{Optical}(\vec{r},t) \\ \lim\limits_{\|\Omega\|\to+\infty} T(\vec{r},t) = 0 \\ \lim\limits_{\|\Omega\|\to+\infty} u(\vec{r},t) = 0 \\ T(\vec{r},t)|_{t=0} = 0 \end{cases}$$

Here, light propagation time is neglected relative to heat propagation. The following equations solve the time-dependent Green's function for the thermal part:

$$\begin{cases} c\rho \dfrac{\partial G_{Thermal}(\vec{r},t;\vec{r'},t')}{\partial t} - k\nabla^2 G_{Thermal}(\vec{r},t;\vec{r'},t') = \delta(\vec{r}-\vec{r'})\delta(t-t') \\ \lim\limits_{\|\Omega\|\to+\infty} G_{Thermal}(\vec{r},t;\vec{r'},t') = 0 \\ G_{Thermal}(\vec{r},t;\vec{r'},t')|_{t<t'} = 0 \end{cases}$$

$$G_{Thermal}(\vec{r},t;\vec{r'},t') = \frac{\kappa}{8k[\pi\kappa(t-t')]^{\frac{3}{2}}} e^{-\frac{(\vec{r}-\vec{r'})^2}{4\kappa(t-t')}}$$

The temperature rise due to this thermal component only depends on two thermal properties: thermal diffusivity (κ) and thermal conductivity (k). For the photothermal part, the

Please cite this article in press as: Wu et al., Analysis and management of thermal loads generated *in vivo* by miniaturized optoelectronic implantable devices, Device (2025), https://doi.org/10.1016/j.device.2025.100898

time-dependent Green's function can be derived by solving the governing equation in two steps:

$$\begin{cases} c\rho\dfrac{\partial G_{Optical}(\vec{r},t;\vec{r}',t')}{\partial t} - k\nabla^2 G_{Optical}(\vec{r},t;\vec{r}',t') = \mu_a G_{OFR}(\vec{r},t;\vec{r}',t') \\ \mu_a G_{OFR}(\vec{r},t;\vec{r}',t') - D\nabla^2 G_{OFR}(\vec{r},t;\vec{r}',t') = \delta(\vec{r},\vec{r}')\delta(t,t') \\ \lim\limits_{\|\Omega\|\to+\infty} G_{OFR}(\vec{r},t;\vec{r}',t') = 0 \\ G_{OFR}(\vec{r},t;\vec{r}',t')|_{t<t'} = 0 \\ \lim\limits_{\|\Omega\|\to+\infty} G_{Optical}(\vec{r},t;\vec{r}',t') = 0 \\ G_{Optical}(\vec{r},t;\vec{r}',t')\big|_{t<t'} = 0 \end{cases}$$

First, we solve for the time-dependent Green's function related to the 3D optical transient propagation:

$$\mu_a G_{OFR}(\vec{r},t;\vec{r}',t') - D\nabla^2 G_{OFR}(\vec{r},t;\vec{r}',t') = \delta(\vec{r},\vec{r}')\delta(t,t')$$
$$\lim_{\|\Omega\|\to+\infty} G_{OFR}(\vec{r},t;\vec{r}',t') = 0$$
$$G_{OFR}(\vec{r},t;\vec{r}',t')|_{t<t'} = 0$$

The corresponding solution is

$$G_{Optical}(\vec{r},t;\vec{r}',t') = \frac{1}{4\pi D\|\vec{r}-\vec{r}'\|}e^{-\mu_{eff}\|\vec{r}-\vec{r}'\|}\delta(t,t')$$

The second step solves the temperature rise by addressing the heat conduction due to optical effects:

$$c\rho\frac{\partial G_{Optical}(\vec{r},t;\vec{r}',t')}{\partial t} - k\nabla^2 G_{Optical}(\vec{r},t;\vec{r}',t') = \mu_a G_{OFR}(\vec{r},t;\vec{r}',t')$$
$$\lim_{\|\Omega\|\to+\infty} G_{Optical}(\vec{r},t;\vec{r}',t') = 0$$
$$G_{Optical}(\vec{r},t;\vec{r}',t')\big|_{t<t'} = 0$$

Using the Green's function method, we calculate the temperature rise generated by the photothermal interaction:

$$G_{Optical}(\vec{r},t;\vec{r}',t') = \int_0^{t^+}\int_\Omega \mu_a G_{OFR}(\vec{r}'',t'';\vec{r}',t')$$
$$G_{Thermal}(\vec{r},t;\vec{r}'',t'')d\Omega''dt''$$

By calculating the integral for this part, we derive the time-dependent Green's function for the photothermal PDE:

$$G_{Optical}(\vec{r},t;\vec{r}',t') = \frac{\kappa\mu_{eff}^2}{8\pi k\|\vec{r}-\vec{r}'\|}\left[e^{\kappa(t-t')\mu_{eff}^2-\mu_{eff}\|\vec{r}'-\vec{r}\|}erfc\right.$$
$$\left(\frac{2\kappa(t-t')\mu_{eff}-\|\vec{r}-\vec{r}'\|}{\sqrt{4\kappa(t-t')}}\right) - e^{\kappa(t-t')\mu_{eff}^2+\mu_{eff}\|\vec{r}'-\vec{r}\|}$$
$$\left.erfc\left(\frac{2\kappa(t-t')\mu_{eff}+\|\vec{r}-\vec{r}'\|}{\sqrt{4\kappa t-t'}}\right)\right]$$

The photothermal temperature rise depends on two thermal properties (κ and k) and one optical property (μ_{eff}). For a general source, the optical fluence rate distribution can be obtained by integrating the Green's function:

$$u(\vec{r},t) = \int_0^{t^+}\int_\Omega G_{OFR}(\vec{r},t;\vec{r}',t')Q_{Optical}(\vec{r}',t')d\Omega'dt'$$

Likewise, the distribution of the temperature rise for the general source under transient conditions is as follows:

$$T_{Optical}(\vec{r},t) = \int_0^{t^+}\int_\Omega G_{Optical}(\vec{r},t;\vec{r}',t')Q_{Optical}(\vec{r}',t')d\Omega'dt'$$

$$T_{Thermal}(\vec{r},t) = \int_0^{t^+}\int_\Omega G_{Thermal}(\vec{r},t;\vec{r}',t')Q_{Thermal}(\vec{r}',t')d\Omega'dt'$$

$$T_{Total}(\vec{r},t) = T_{Optical}(\vec{r},t)+T_{Thermal}(\vec{r},t)$$

For specific cases, such as a pulsed source, which is commonly used in optogenetic stimulations, the corresponding source term can be further written as

$$Q_{Optical}(\vec{r}',t') = P_{Optical}(\vec{r}')W(t',DC,\tau)$$

$$Q_{Thermal}(\vec{r}',t') = P_{Thermal}(\vec{r}')W(t',DC,\tau)$$

Here, $W(t')$ is a step function defined by pulsing properties:

$$W(t',DC,\tau) = \begin{cases} 1 & n\tau < t' \le DC\tau + n\tau \\ 0 & DC\tau + n\tau < t' \le \tau + n\tau \end{cases}$$

The corresponding optical fluence rate can be given by

$$u(\vec{r},t,DC,\tau) = \frac{1}{4\pi D\|\vec{r}-\vec{r}'\|}e^{-\mu_{eff}\|\vec{r}-\vec{r}'\|}W(t,DC,\tau)$$

The corresponding temperature rise can be given by

$$T_{Optical\_Pulsed}(\vec{r},t,DC,\tau) = Pulsed\left(T_{Optical\_Constant}\right.$$

$$\left.(\vec{r},t-n\tau),DC,\tau\right) = \sum_{n=0}^{+\infty}H(t-n\tau)T_{Optical\_Constant}$$

$$(\vec{r},t-n\tau) - H(t-(DC\tau+n\tau))T_{Optical\_Constant}$$

$$(\vec{r},t-(DC\tau+n\tau))$$

$$T_{Thermal\_Pulsed}(\vec{r},t,DC,\tau) = Pulsed\left(T_{Thermal\_Constant}(\vec{r},t),DC,\tau\right)$$

$$= \sum_{n=0}^{+\infty}H(t-n\tau)T_{Thermal\_Constant}(\vec{r},t-n\tau) - H(t-(DC\tau+n\tau))$$

$$T_{Thermal\_Constant}(\vec{r},t-(DC\tau+n\tau))$$

$$T_{Total\_Pulsed}(\vec{r},t,DC,\tau) = T_{Thermal\_Pulsed}(\vec{r},t,DC,\tau) + T_{Optical\_Pulsed}(\vec{r},t,DC,\tau)$$

Here, $H(x)$ is the well-known Heaviside function. $T_{Optical\_Constant}$ and $T_{Thermal\_Constant}$ are the transient temperature rises caused by a constant source term:

$$Q_{Optical}(\vec{r}') = P_{Optical}(\vec{r}')$$

$$Q_{Thermal}(\vec{r}') = P_{Thermal}(\vec{r}')$$

For a constant source term, the temperature rise may be determined using the following equations:

$$T_{Optical\_Constant}(\vec{r},t) = \int_0^{t^+}\int_\Omega G_{Optical}(\vec{r},t;\vec{r}',t')P_{Optical}(\vec{r}')d\Omega'dt'$$

$$= \int_\Omega G_{Optical\_Constant}(\vec{r},t;\vec{r}',t')P_{Optical}(\vec{r}')d\Omega'$$

$$G_{Optical\_Constant}(\vec{r},t;\vec{r}') = \int_0^{t^+}G_{Optical}(\vec{r},t;\vec{r}')dt'$$

$$T_{Thermal\_Constant}(\vec{r},t) = \int_0^{t^+}\int_\Omega G_{Thermal}(\vec{r},t;\vec{r}',t')P_{Thermal}(\vec{r}')d\Omega'dt'$$

$$= \int_\Omega G_{Thermal\_Constant}(\vec{r},t;\vec{r}',t')P_{Thermal}(\vec{r}')d\Omega'$$

$$G_{Thermal\_Constant}(\vec{r},t;\vec{r}') = \int_0^{t^+}G_{Thermal}(\vec{r},t;\vec{r}')dt'$$

$$G_{Thermal\_Constant}(\vec{r},t;\vec{r}') = \frac{1}{4\pi k\|\vec{r}-\vec{r}'\|}erfc\left(\frac{\|\vec{r}-\vec{r}'\|}{\sqrt{4\kappa t}}\right)$$

$$G_{Optical\_Constant}(\vec{r},t;\vec{r}') = \frac{1}{8\pi k\|\vec{r}-\vec{r}'\|}\left[e^{-\mu_{eff}\|\vec{r}-\vec{r}'\|}e^{\kappa\mu_{eff}{}^2t}erfc\right.$$

$$\left(\frac{2\kappa t\mu_{eff}-\|\vec{r}-\vec{r}'\|}{\sqrt{4\kappa t}}\right) - e^{\mu_{eff}\|\vec{r}-\vec{r}'\|}e^{\kappa\mu_{eff}{}^2t}erfc$$

$$\left.\left(\frac{2\kappa t\mu_{eff}+\|\vec{r}-\vec{r}'\|}{\sqrt{4\kappa t}}\right) + 2erfc\left(\frac{\|\vec{r}-\vec{r}'\|}{\sqrt{4\kappa t}}\right) - 2e^{-\mu_{eff}\|\vec{r}-\vec{r}'\|}\right]$$

Specifically for a constant point source, the following equations apply:

$$Q_{Optical}(\vec{r}',\vec{r}'') = P_{Optical}\delta(\vec{r}',\vec{r}'')$$

$$Q_{Thermal}(\vec{r}',\vec{r}'') = P_{Thermal}\delta(\vec{r}',\vec{r}'')$$

$$u_{Point}(\vec{r},t;\vec{r}'') = \frac{P_{Optical}}{4\pi D\|\vec{r}-\vec{r}''\|}e^{-\mu_{eff}\|\vec{r}-\vec{r}''\|}$$

$$T_{Optical\_Point}(\vec{r},t;\vec{r}'') = = \int_\Omega G_{Optical\_Constant}(\vec{r},t;\vec{r}')$$

$$P_{Optical}\delta(\vec{r}',\vec{r}'')d\Omega' = P_{Optical}G_{Thermal\_Constant}(\vec{r},t;\vec{r}'')$$

$$T_{Thermal\_Point}(\vec{r},t;\vec{r}'') = \int_\Omega G_{Thermal\_Constant}(\vec{r},t;\vec{r}')$$

$$P_{Thermal}\delta(\vec{r}',\vec{r}'')d\Omega' = P_{Thermal}G_{Thermal\_Constant}(\vec{r},t;\vec{r}'')$$

Please cite this article in press as: Wu et al., Analysis and management of thermal loads generated *in vivo* by miniaturized optoelectronic implantable devices, Device (2025), https://doi.org/10.1016/j.device.2025.100898

$$T_{Total\_Point}(\vec{r},t;\vec{r''}) = T_{Optical\_Point}(\vec{r},t;\vec{r''}) + T_{Thermal\_Point}(\vec{r},t;\vec{r''})$$

As $t\rightarrow+\infty$, we have the following equation showing $T_{Optical\_Point}(\vec{r},t;\vec{r''})$ is self-consistent:

$$\lim_{t\rightarrow+\infty} T_{Optical\_Point}(\vec{r},t;\vec{r''}) = T_{Optical\_Point}(\vec{r},\vec{r''})$$

Here, $T_{Optical\_Point}(\vec{r},\vec{r''})$ is the steady-state temperature rise for a point source.

When we set $\vec{r''} = 0$, we can get the optical fluence rate and temperature rise caused by a constant point source at the origin:

$$u_{Point}(r) = \frac{P_{Optical}}{4\pi D r} e^{-\mu_{eff} r}$$

$$T_{Thermal}(r,t) = \frac{P_{Thermal}}{4\pi k r} erfc\left(\frac{r}{\sqrt{4\kappa t}}\right)$$

$$T_{Optical}(r,t) = \frac{P_{Optical}}{8\pi k r}\left[e^{-\mu_{eff} r} e^{\kappa\mu_{eff}{}^2 t} erfc\left(\frac{2\kappa t\mu_{eff} - r}{\sqrt{4\kappa t}}\right) - e^{\mu_{eff} r} e^{\kappa\mu_{eff}{}^2 t} erfc\left(\frac{2\kappa t\mu_{eff} + r}{\sqrt{4\kappa t}}\right) + 2erfc\left(\frac{r}{\sqrt{4\kappa t}}\right) - 2e^{-\mu_{eff} r}\right]$$

$$T_{Total}(r,t) = T_{Optical}(r,t) + T_{Thermal}(r,t)$$

The above solutions are based on the isotropic radiation pattern. For other anisotropic sources, such as Lambertian, fiber optics or laser sources, resulting radiation patterns may be obtained using a scaling factor (*SF*), which is a function of space and time:

$$u(\vec{r},t;\vec{r''}) = SF_{OFR} u_{Point}(\vec{r},t;\vec{r''})$$

$$T_{Optical}(\vec{r},t;\vec{r''}) = SF_{Optical} T_{Optical\_Point}(\vec{r},t;\vec{r''})$$

$$T_{Thermal}(\vec{r},t;\vec{r''}) = SF_{Thermal} T_{Thermal\_Point}(\vec{r},t;\vec{r''})$$

$$T_{Total}(\vec{r},t;\vec{r''}) = T_{Thermal}(\vec{r},t;\vec{r''}) + T_{Optical}(\vec{r},t;\vec{r''})$$

For the Lambertian source, which represents typical optoelectronic light sources such as LEDs, the solution can be represented using dimensionless parameters:

$$u_{LED}(\vec{r},t) = \frac{P_{Optical}}{Dh} g_{OFR}(x/w, y/w, z/w, \mu_{eff} w, l/w, h/w)$$

$$T_{Thermal\_LED}(\vec{r},t) = \frac{qwl}{kh} g_{Thermal}$$

$$(\kappa t/l^2, x/w, y/w, z/w, l/w, h/w)$$

$$T_{Optical\_LED}(\vec{r},t) = \frac{qwl}{kh} g_{Optical}$$

$$(\kappa\mu_{eff}{}^2 t, x/w, y/w, z/w, \mu_{eff} w, l/w, h/w)$$

$$T_{Total\_LED}(\vec{r},t) = T_{Thermal\_LED}(\vec{r},t) + T_{Optical\_LED}(\vec{r},t)$$

$$= \frac{qwl}{kh} g_{Total}(\kappa\mu_{eff}{}^2 t, x/w, y/w, z/w, \mu_{eff} w, l/w, h/w)$$

$$T_{Total\_LED\_Pulsed}(\vec{r},t) = T_{Thermal\_LED\_Pulsed}(\vec{r},t,DC,\tau)$$

$$+ T_{Optical\_LED\_Pulsed}(\vec{r},t,DC,\tau) = Pulsed\left(T_{Thermal\_LED}(\vec{r},t),DC,\tau\right)$$

$$+ Pulsed\left(T_{Optical\_LED}(\vec{r},t),DC,\tau\right) = \frac{qwl}{kh} g_{Total\_Pulsed}$$

$$(\kappa\mu_{eff}{}^2 t, x/w, y/w, z/w, \mu_{eff} w, l/w, h/w, DC, \kappa\mu_{eff}{}^2\tau)$$

Here, q is the power density. To consider the effects of varying probe geometries and materials, the above solutions can be further modified using the appropriate scaling factor:

$$u(\vec{r},t) = SF_{OFR} u_{LED}(\vec{r},t)$$

$$T_{Thermal}(\vec{r},t) = SF_{Thermal} T_{Thermal\_LED}(\vec{r},t)$$

$$T_{Optical}(\vec{r},t) = SF_{Optical} T_{Optical\_LED}(\vec{r},t)$$

$$T_{Total}(\vec{r},t) = T_{Thermal}(\vec{r},t) + T_{Optical}(\vec{r},t)$$

Optical simulations

Optical simulations for transcranial optogenetic stimulation were performed using the Monte Carlo method.[74] For simulations of radiation patterns, the simulation volume consisted of a cubic grid with $(200)^3$ voxels, each voxel measuring $(25\ \mu m)^3$, covering a total volume of $(5\ mm)^3$. For simulations involving simple and realistic probes, the simulation volume consisted of a cubic grid with $(500)^3$ voxels, each voxel measuring $(10\ \mu m)^3$, covering a total volume of $(5\ mm)^3$.The illumination sources used here, in order of increasing degree of anisotropy, are isotropic, Lambertian, fiber, and laser. The corresponding expressions can be written as

$$L(\theta) = L_0 R(\theta)$$

Isotropic:

$$R(\theta) = 1$$

Lambertian:

$$R(\theta) = \cos\theta$$

Fiber:

$$R(\theta) = \begin{cases} 1, -\beta \le \theta \le \beta \\ 0, else \end{cases}$$

Laser:

$$R(\theta) = \begin{cases} 1, \theta = 0 \\ 0, else \end{cases}$$

Here, $L(\theta)$ is the optical intensity. θ is the angle between the irradiation direction and the vertical direction. Both point and

Please cite this article in press as: Wu et al., Analysis and management of thermal loads generated *in vivo* by miniaturized optoelectronic implantable devices, Device (2025), https://doi.org/10.1016/j.device.2025.100898

cuboid sources were investigated with the sources positioned in the center of the simulation volume. Optical properties such as absorption and scattering coefficients, as well as refractive index, that were used in the simulation are detailed in Table S1. The resulting optical fluence rate distribution at 1-mW irradiation was visualized using MATLAB.

Thermal FEA model. Temperature distributions were modeled to account for both Joule heating of the device and optically induced thermal effects. The optical fluence rate is obtained from optical simulation. The temperature boundary condition was set as zero, and the tissue size used was large enough to be approximated as an infinite medium. Abaqus software was used to solve the thermal-optical coupled equation with finite-element methods,[75,76] utilizing linear tetrahedral elements with a minimum edge length of 10 μm. Material properties, including thermal conductivity, heat capacity, and mass density, are detailed in Table S2.

Because the tissue volume is sufficiently large, the temperature at the boundary approaches the ambient temperature as heat propagates. Thus, we impose a constant boundary condition in our model. By the linearity of the governing heat-conduction equation, applying a zero-temperature boundary yields the temperature rise relative to baseline ($T = \Delta T$), whereas applying an ambient-temperature boundary yields the absolute temperature profile. Notably, in smaller tissue volumes, the assumption of an infinite medium may lead to deviations in predicted peak temperatures depending on the actual boundary condition. Such limitations should be considered when interpreting results under constrained geometries.

Fabrication of optoelectronic probe. Electrical traces and pads for the μ-ILED were created using laser ablation on a flexible Cu/PI/Cu sheet (18 μm/75 μm/18 μm, Pyralux AP8535R, DuPont). The blue μ-ILED (TR2227, CREE) was soldered onto the probe using a heat gun set to a low speed and temperature (230°C–250°C). The polydimethylsiloxane sheet (PDMS 200 μm, Limitless Shielding) was laser cut to form the chamber for the μ-ILED encapsulation using LPKF PhotoLaser R (LPKF Laser & Electronics SE, DE). Subsequently, the PDMS chamber was aligned with the electrical traces and PDMS silicone elastomer (Dow SYLGARD 184) was used to attach the thermistor to the PDMS or air-encapsulated μ-ILEDs. Electrical wires (34 AWG) were soldered for electrical connections. The μ-ILED was powered by a high-resolution current source (Keithley model 6221) for further characterization of thermal effects.

Thermistor fabrication and thermal characterization. A thin-film thermistor was fabricated using photolithography to pattern a layer of gold between two insulating layers of PI. A silicon wafer was first spin-coated with a layer of polymethyl methacrylate (PMMA, 500 nm) followed by PI (5 μm). A conductive film of 20 nm of titanium and 100 nm of gold was then deposited on the PI layer, followed by a photoresist layer patterned using a maskless aligner. After wet etching to define the sensor geometry, a top layer of PI (5 μm) was deposited by spin-casting as before. A film of 60 nm of Cu was deposited on the PI layer to act as a mask for the subsequent etching of PI. Thereafter, a photoresist layer was patterned using a maskless aligner, followed by wet etching, reactive ion etching of the PI, and finally the removal of the Cu mask through wet etching. The thermistors were then transferred onto water-soluble tape that was dissolved in deionized (DI) water before the thermistors were attached to the optoelectronic probes, with the serpentine resistive element positioned directly above the μ-ILED. This placement enabled localized temperature detection at the device-tissue interface. The thermistor's geometry and material properties were incorporated into the finite-element model to account for potential thermal artifacts and maintain spatial consistency with experimental measurements. Care was taken to avoid direct electrical or optical contact between the thermistor and μ-ILED to minimize self-heating and other thermal artifacts. Electrical connections were established using silver paint, and UV resin was applied to provide additional mechanical support and electrical insulation. The resulting thermistor on optoelectronic probe was encapsulated in 10-μm-thick parylene C using chemical vapor deposition. Temperature responses were measured in air, ethanol, and DI water using a digital multimeter (USB-4065, National Instruments), and calibration of thermistors was performed with a thermometer (HH374, OMEGA) in controlled water bath over a temperature range of 30°C–60°C. The operating voltages of μ-ILED remained consistent at 2.7–2.8 V in all tested configurations at a driving current of 2 mA.

Optoelectronic characterization. The test blue μ-ILED was mounted on a PI-filament probe and soldered to the electrical traces using the same methods described above. We used a high-resolution current source (Keithley 6221, Tektronix) to drive the μ-ILED. An integrating sphere (FOIS-1, Ocean Insight) and a spectrometer (HL-3 plus, Ocean Insight) defined the spectral irradiance to allow calculation of the net optical power as a function of input current. The current-voltage (IV) characteristics were obtained using a high-resolution digital multimeter (USB-4065, National Instruments).

Microscale computed tomography imaging. Mice were given an intraperitoneal (i.p.) injection of iohexol (iodine-based, CT contrast agent) 15 min before euthanasia. After euthanasia, animals were scanned using a microPET/CT system (Mediso nanoScan). Scans were conducted with medium magnification, a 33-μm focal spot, and 1×1 binning, acquiring 720 projections over a full circle with a 90-ms exposure time. X-ray power was set at 70 kVp for imaging, and the projection data were reconstructed into 34-μm voxels.

Geometric modeling. The geometric models of cranial structures were reconstructed based on the microCT scans using the Amira software. The resulting geometric models of the organs were exported as STL files and further processed in Geomagic and SpaceClaim to reduce noise and artifacts. These models were processed in Abaqus and converted into voxelized meshes for use in optical and thermal simulations.

Stereotactic implantation. Mice were anesthetized with either isoflurane (3% induction, 1.5%–2% maintenance) or a ketamine-xylazine mixture (100:12.5 mg/kg) and received analgesics (ketoprofen, meloxicam, or buprenorphine). They were positioned in a stereotaxic frame (David Kopf Instruments). Implantation coordinates were slightly adjusted based on mouse age and size, with typical coordinates for the dorsal striatum being −0.5 mm (anterior-posterior), +2.0 mm (medial-lateral), and −3.0 mm (dorsal-ventral).

Open-field locomotion test. We assessed locomotor activity by placing mice in a 30 × 30-cm open-field arena illuminated with infrared light. The mice explored the arena freely for 30 min while we recorded their movements at 25 frames per second using a Raspberry Pi camera. During pulsed optical stimulation sessions, we applied a pulsatile profile with 2-ms pulse width and a peak electric current of 30 mA, which corresponded to a total power load of 93.2 mW, to the implanted optimized optoelectronic probe through tethered thin Cu wires. The standard optoelectronic probe operated with a peak electric current of 8 mA, which corresponded to a total power load of 23.6 mW. For each session, the μ-ILED was subjected to 30-s heating and 30-s cooling phases over 30 min. Baseline sessions were conducted without stimulation. Using Toxtrac software,[77] we tracked the positions of the animals based on their body centers and calculated the distance traveled and exploration rate for each session.

Quantification and statistical analysis

Statistical analyses

Required sample sizes were estimated based on previous publications and experience.[78–80] The number of replicates was reported, and several internal replications are present in the study. No data were excluded after analyses. Animals were randomly assigned to treatment groups. Group statistical analyses were done using GraphPad Prism software (GraphPad, LaJolla, CA). For sample size *n*, the number of technical and biological replicates are provided. All data are expressed as mean ± SD or individual plots. Probabilities are expressed as aggregate probabilities within individuals. For multiple group comparisons, two-way analysis of variance (ANOVA) test were used for normally distributed data, followed by post hoc analyses. $p < 0.05$ was considered statistically significant.

RESOURCE AVAILABILITY

Lead contact

Further information and requests for resources and reagents should be directed to and will be fulfilled by the lead contact, John A. Rogers (jrogers@northwestern.edu).

Materials availability

This study did not generate new unique reagents.

Data and code availability

- This study did not generate code, but datasets related to the current study are available from the lead contact upon request.
- Design files and models are available at https://doi.org/10.5281/zenodo.15359658.

ACKNOWLEDGMENTS

This work made use of the NUFAB facility of Northwestern University's NUANCE Center, which has received support from the SHyNE Resource (NSF ECCS-2025633), the IIN, and Northwestern's MRSEC program (NSF DMR-2308691). MicroCT imaging work was performed at the Northwestern University Center for Advanced Molecular Imaging (RRID:SCR_021192) generously supported by NCI CCSG P30 CA060553 awarded to the Robert H. Lurie Comprehensive Cancer Center. Some schematic illustrations used materials created by BioRender.com. This work was funded by the Querrey-Simpson Institute for Bioelectronics (M.W., P.J.Y.F., A.I.E., Y. Wang, J.F., J. G., X.L., D.H., L.Z., T.Y., J.L., G.W., Y.Y., A.V.-G., Y.H., and J.A.R.), NINDS/BRAIN Initiative 1U01NS131406 (Y.K., J.A.R., and M.W.), NC State University Start-up fund 201473-02139 (A.V.-G.), and 2T32MH06756 (J.Z.).

AUTHOR CONTRIBUTIONS

Conceptualization, M.W., K.Z., A.V.-G., Y.H., and J.A.R.; methodology, M.W., K.Z., P.J.Y.F., A.V.-G., A.I.E., Y.H., and J.A.R.; theoretical simulations, K.Z., H. Z., S.L., Z.L., and Y.H.; investigation, M.W., K.Z., P.J.Y.F., H.Z., A.I.E., Y. Wang, J.F., S.L., J.G., X.L., D.H., L.Z., E.A.W., T.Y., J.Z., J.L., Z.L., Y. Wei, Y.Y., C.R.H., Y.K., R.A., and A.V.-G.; software, P.J.Y.F., Y. Wang, and G.W.; formal analysis, M.W., K.Z., and P.J.Y.F.; validation, M.W., K.Z., P.J.Y.F., and H.Z.; data curation, M.W. and P.J.Y.F.; visualization, M.W., K.Z., P.J.Y.F., and J.Z.; supervision, A.V.-G., Y.H., and J.A.R.; funding acquisition, Y.K., Y.H., and J.A.R.; writing – original draft, M.W., K.Z., P.J.Y.F., and A.V.-G.; writing – review & editing, M.W., K.Z., P.J.Y.F., H.Z., Y.K., A.V.-G., Y.H., and J.A.R.

DECLARATION OF INTERESTS

The authors declare no competing interests.

SUPPLEMENTAL INFORMATION

Supplemental information can be found online at https://doi.org/10.1016/j.device.2025.100898.

Received: May 8, 2025
Revised: July 17, 2025
Accepted: July 25, 2025

REFERENCES

1. Wu, J., Lin, H., Moss, D.J., Loh, K.P., and Jia, B. (2023). Graphene oxide for photonics, electronics and optoelectronics. Nat. Rev. Chem *7*, 162–183. https://doi.org/10.1038/s41570-022-00458-7.
2. Balakrishnan, G., Song, J., Mou, C., and Bettinger, C.J. (2022). Recent Progress in Materials Chemistry to Advance Flexible Bioelectronics in Medicine. Adv. Mater. *34*, 2106787. https://doi.org/10.1002/adma.202106787.
3. Heng, W., Solomon, S., and Gao, W. (2022). Flexible Electronics and Devices as Human–Machine Interfaces for Medical Robotics. Adv. Mater. *34*, 2107902. https://doi.org/10.1002/adma.202107902.
4. Ko, H.C., Stoykovich, M.P., Song, J., Malyarchuk, V., Choi, W.M., Yu, C.-J., Geddes, J.B., III, Xiao, J., Wang, S., Huang, Y., and Rogers, J.A. (2008). A hemispherical electronic eye camera based on compressible silicon optoelectronics. Nature *454*, 748–753. https://doi.org/10.1038/nature07113.
5. Yoon, J., Jo, S., Chun, I.S., Jung, I., Kim, H.-S., Meitl, M., Menard, E., Li, X., Coleman, J.J., Paik, U., and Rogers, J.A. (2010). GaAs photovoltaics and optoelectronics using releasable multilayer epitaxial assemblies. Nature *465*, 329–333. https://doi.org/10.1038/nature09054.
6. Li, P., Zhang, J., Hayashi, H., Yue, J., Li, W., Yang, C., Sun, C., Shi, J., Huberman-Shlaes, J., Hibino, N., and Tian, B. (2024). Monolithic silicon for high spatiotemporal translational photostimulation. Nature *626*, 990–998. https://doi.org/10.1038/s41586-024-07016-9.
7. Zhang, Z., Wang, W., Jiang, Y., Wang, Y.-X., Wu, Y., Lai, J.-C., Niu, S., Xu, C., Shih, C.-C., Wang, C., et al. (2022). High-brightness all-polymer stretchable LED with charge-trapping dilution. Nature *603*, 624–630. https://doi.org/10.1038/s41586-022-04400-1.
8. Kim, R.-H., Kim, D.-H., Xiao, J., Kim, B.H., Park, S.-I., Panilaitis, B., Ghaffari, R., Yao, J., Li, M., Liu, Z., et al. (2010). Waterproof AlInGaP optoelectronics on stretchable substrates with applications in biomedicine and robotics. Nat. Mater. *9*, 929–937. https://doi.org/10.1038/nmat2879.

9. Kim, T. -i., McCall, J.G., Jung, Y.H., Huang, X., Siuda, E.R., Li, Y., Song, J., Song, Y.M., Pao, H.A., Kim, R.-H., et al. (2013). Injectable, Cellular-Scale Optoelectronics with Applications for Wireless Optogenetics. Science *340*, 211–216. https://doi.org/10.1126/science.1232437.

10. Park, S.I., Brenner, D.S., Shin, G., Morgan, C.D., Copits, B.A., Chung, H. U., Pullen, M.Y., Noh, K.N., Davidson, S., Oh, S.J., et al. (2015). Soft, stretchable, fully implantable miniaturized optoelectronic systems for wireless optogenetics. Nat. Biotechnol. *33*, 1280–1286. https://doi.org/10.1038/nbt.3415.

11. Lu, L., Gutruf, P., Xia, L., Bhatti, D.L., Wang, X., Vazquez-Guardado, A., Ning, X., Shen, X., Sang, T., Ma, R., et al. (2018). Wireless optoelectronic photometers for monitoring neuronal dynamics in the deep brain. Proc. Natl. Acad. Sci. USA *115*, E1374–E1383. https://doi.org/10.1073/pnas.1718721115.

12. Zhang, H., Gutruf, P., Meacham, K., Montana, M.C., Zhao, X., Chiarelli, A. M., Vázquez-Guardado, A., Norris, A., Lu, L., Guo, Q., et al. (2019). Wireless, battery-free optoelectronic systems as subdermal implants for local tissue oximetry. Sci. Adv. *5*. https://doi.org/10.1126/sciadv.aaw0873.

13. Taal, A.J., Uguz, I., Hillebrandt, S., Moon, C.-K., Andino-Pavlovsky, V., Choi, J., Keum, C., Deisseroth, K., Gather, M.C., and Shepard, K.L. (2023). Optogenetic stimulation probes with single-neuron resolution based on organic LEDs monolithically integrated on CMOS. Nat. Electron. *6*, 669–679. https://doi.org/10.1038/s41928-023-01013-y.

14. Pollmann, E.H., Yin, H., Uguz, I., Dubey, A., Wingel, K.E., Choi, J.S., Moazeni, S., Gilhotra, Y., Andino-Pavlovsky, V., Banees, A., et al. (2024). A subdural CMOS optical device for bidirectional neural interfacing. Nat. Electron. *7*, 829–841. https://doi.org/10.1038/s41928-024-01209-w.

15. Yin, J., Wang, S., Xiao, X., Manshaii, F., Scott, K., and Chen, J. (2025). Leveraging biomimetic materials for bioelectronics. Matter *8*, 101961. https://doi.org/10.1016/j.matt.2025.101961.

16. Hsissou, R., Seghiri, R., Benzekri, Z., Hilali, M., Rafik, M., and Elharfi, A. (2021). Polymer composite materials: A comprehensive review. Compos. Struct. *262*, 113640. https://doi.org/10.1016/j.compstruct.2021.113640.

17. Shin, G., Gomez, A.M., Al-Hasani, R., Jeong, Y.R., Kim, J., Xie, Z., Banks, A., Lee, S.M., Han, S.Y., Yoo, C.J., et al. (2017). Flexible Near-Field Wireless Optoelectronics as Subdermal Implants for Broad Applications in Optogenetics. Neuron *93*, 509–521.e3. https://doi.org/10.1016/j.neuron.2016.12.031.

18. Yang, Y., Wu, M., Vázquez-Guardado, A., Wegener, A.J., Grajales-Reyes, J.G., Deng, Y., Wang, T., Avila, R., Moreno, J.A., Minkowicz, S., et al. (2021). Wireless multilateral devices for optogenetic studies of individual and social behaviors. Nat. Neurosci. *24*, 1035–1045. https://doi.org/10.1038/s41593-021-00849-x.

19. Ausra, J., Wu, M., Zhang, X., Vázquez-Guardado, A., Skelton, P., Peralta, R., Avila, R., Murickan, T., Haney, C.R., Huang, Y., et al. (2021). Wireless, battery-free, subdermally implantable platforms for transcranial and long-range optogenetics in freely moving animals. Proc. Natl. Acad. Sci. USA *118*. https://doi.org/10.1073/PNAS.2025775118.

20. Owen, S.F., Liu, M.H., and Kreitzer, A.C. (2019). Thermal constraints on in vivo optogenetic manipulations. Nat. Neurosci. *22*, 1061–1065. https://doi.org/10.1038/s41593-019-0422-3.

21. Thomsen, S. (1991). PATHOLOGIC ANALYSIS OF PHOTOTHERMAL AND PHOTOMECHANICAL EFFECTS OF LASER–TISSUE INTERACTIONS. Photochem. Photobiol. *53*, 825–835. https://doi.org/10.1111/j.1751-1097.1991.tb09897.x.

22. Nakamura, S. (1998). The Roles of Structural Imperfections in InGaN-Based Blue Light-Emitting Diodes and Laser Diodes. Science *281*, 956–961. https://doi.org/10.1126/science.281.5379.956.

23. Stujenske, J.M., Spellman, T., and Gordon, J.A. (2015). Modeling the Spatiotemporal Dynamics of Light and Heat Propagation for In Vivo Optogenetics. Cell Rep. *12*, 525–534. https://doi.org/10.1016/j.celrep.2015.06.036.

24. Kim, T., Kadji, H., Whalen, A.J., Ashourvan, A., Freeman, E., Fried, S.I., Tadigadapa, S., and Schiff, S.J. (2022). Thermal effects on neurons during stimulation of the brain. J. Neural. Eng. *19*, 056029. https://doi.org/10.1088/1741-2552/ac9339.

25. Gysbrechts, B., Wang, L., Trong, N.N.D., Cabral, H., Navratilova, Z., Battaglia, F., Saeys, W., and Bartic, C. (2016). Light distribution and thermal effects in the rat brain under optogenetic stimulation. J. Biophoton. *9*, 576–585. https://doi.org/10.1002/jbio.201500106.

26. Dong, N., Berlinguer-Palmini, R., Soltan, A., Ponon, N., O'Neil, A., Travelyan, A., Maaskant, P., Degenaar, P., and Sun, X. (2018). Opto-electrothermal optimization of photonic probes for optogenetic neural stimulation. J Biophotonics *11*, e201700358. https://doi.org/10.1002/jbio.201700358.

27. Picot, A., Dominguez, S., Liu, C., Chen, I.-W., Tanese, D., Ronzitti, E., Berto, P., Papagiakoumou, E., Oron, D., Tessier, G., et al. (2018). Temperature Rise under Two-Photon Optogenetic Brain Stimulation. Cell Rep. *24*, 1243–1253.e5. https://doi.org/10.1016/j.celrep.2018.06.119.

28. Venkatachalam, K., and Montell, C. (2007). TRP Channels. Annu. Rev. Biochem. *76*, 387–417. https://doi.org/10.1146/annurev.biochem.75.103004.142819.

29. Voets, T., Droogmans, G., Wissenbach, U., Janssens, A., Flockerzi, V., and Nilius, B. (2004). The principle of temperature-dependent gating in cold- and heat-sensitive TRP channels. Nature *430*, 748–754. https://doi.org/10.1038/nature02732.

30. Schneider, E.R., Anderson, E.O., Gracheva, E.O., and Bagriantsev, S.N. (2014). Temperature Sensitivity of Two-Pore (K2P) Potassium Channels. In Current Topics in Membranes (Academic Press), pp. 113–133. https://doi.org/10.1016/B978-0-12-800181-3.00005-1.

31. Irvine, L.A., Saleet Jafri, M., and Winslow, R.L. (1999). Cardiac Sodium Channel Markov Model with Temperature Dependence and Recovery from Inactivation. Biophys. J. *76*, 1868–1885. https://doi.org/10.1016/S0006-3495(99)77346-7.

32. Wu, Y., Wang, Q., Granger, J., Reyes Gaido, O., Lopez-Cecetaite, G., Aguilar, E.N., Ludwig, A., Moroni, A., Bianchet, M.A., and Anderson, M. E. (2025). HCN4 channels sense temperature and determine heart rate responses to heat. Nat. Commun. *16*, 2102. https://doi.org/10.1038/s41467-025-57358-9.

33. Lindquist, S., and Craig, E.A. (1988). THE HEAT-SHOCK PROTEINS. Annu. Rev. Genet. *22*, 631–677. https://doi.org/10.1146/annurev.ge.22.120188.003215.

34. Thakur, N., Ray, A.P., Jin, B., Afsharian, N.P., Lyman, E., Gao, Z.-G., Jacobson, K.A., and Eddy, M.T. (2024). Membrane mimetic-dependence of GPCR energy landscapes. Structure *32*, 523–535.e5. https://doi.org/10.1016/j.str.2024.01.013.

35. Poirier, D.R., and Geiger, G.H. (2016). Conduction of Heat in Solids. In Transport Phenomena in Materials Processing (Cham: Springer), pp. 281–327. https://doi.org/10.1007/978-3-319-48090-9_9.

36. Mesradi, M., Genoux, A., Cuplov, V., Abi Haidar, D., Jan, S., Buvat, I., and Pain, F. (2013). Experimental and analytical comparative study of optical coefficient of fresh and frozen rat tissues. J. Biomed. Opt. *18*, 117010. https://doi.org/10.1117/1.JBO.18.11.117010.

37. Emiliani, V., Entcheva, E., Hedrich, R., Hegemann, P., Konrad, K.R., Lüscher, C., Mahn, M., Pan, Z.-H., Sims, R.R., Vierock, J., and Yizhar, O. (2022). Optogenetics for light control of biological systems. Nat. Rev. Methods Primers *2*, 55. https://doi.org/10.1038/s43586-022-00136-4.

38. Simpson, E.H., Akam, T., Patriarchi, T., Blanco-Pozo, M., Burgeno, L.M., Mohebi, A., Cragg, S.J., and Walton, M.E. (2024). Lights, fiber, action! A primer on in vivo fiber photometry. Neuron *112*, 718–739. https://doi.org/10.1016/j.neuron.2023.11.016.

39. Zhou, Z.C., Gordon-Fennell, A., Piantadosi, S.C., Ji, N., Smith, S.L., Bruchas, M.R., and Stuber, G.D. (2023). Deep-brain optical recording of neural dynamics during behavior. Neuron *111*, 3716–3738. https://doi.org/10.1016/j.neuron.2023.09.006.

40. Deisseroth, K. (2011). Optogenetics. Nat. Methods *8*, 26–29. https://doi.org/10.1038/nmeth.f.324.

41. Tang, X., Shen, H., Zhao, S., Li, N., and Liu, J. (2023). Flexible brain–computer interfaces. Nat. Electron. *6*, 109–118. https://doi.org/10.1038/s41928-022-00913-9.

42. Zhou, L., Wu, Z., Sun, M., Park, J., Han, M., Wang, M., Yu, J., Di, Z., Mei, Y., Bai, W., et al. (2023). Flexible, ultrathin bioelectronic materials and devices for chronically stable neural interfaces. Brain-X *1*. https://doi.org/10.1002/brx2.47.

43. Sahasrabudhe, A., Rupprecht, L.E., Orguc, S., Khudiyev, T., Tanaka, T., Sands, J., Zhu, W., Tabet, A., Manthey, M., and Allen, H., et al. (2024). Multifunctional microelectronic fibers enable wireless modulation of gut and brain neural circuits. Nat. Biotechnol. *42*, 892–904. https://doi.org/10.1038/s41587-023-01833-5.

44. Liu, X., Rao, S., Chen, W., Felix, K., Ni, J., Sahasrabudhe, A., Lin, S., Wang, Q., Liu, Y., He, Z., et al. (2023). Fatigue-resistant hydrogel optical fibers enable peripheral nerve optogenetics during locomotion. Nat. Methods *20*, 1802–1809. https://doi.org/10.1038/s41592-023-02020-9.

45. Lacour, S.P., Courtine, G., and Guck, J. (2016). Materials and technologies for soft implantable neuroprostheses. Nat. Rev. Mater. *1*, 16063. https://doi.org/10.1038/natrevmats.2016.63.

46. Valvano, J.W., Cochran, J.R., and Diller, K.R. (1985). Thermal conductivity and diffusivity of biomaterials measured with self-heated thermistors. Int. J. Thermophys. *6*, 301–311. https://doi.org/10.1007/BF00522151.

47. Mohammadi, A., Bianchi, L., Asadi, S., and Saccomandi, P. (2021). Measurement of Ex Vivo Liver, Brain and Pancreas Thermal Properties as Function of Temperature. Sensors *21*, 4236. https://doi.org/10.3390/s21124236.

48. Efimov, A.I., Hibberd, T.J., Wang, Y., Wu, M., Zhang, K., Ting, K., Madhvapathy, S., Lee, M.-K., Kim, J., Kang, J., et al. (2024). Remote optogenetic control of the enteric nervous system and brain-gut axis in freely-behaving mice enabled by a wireless, battery-free optoelectronic device. Biosens. Bioelectron. *258*, 116298. https://doi.org/10.1016/j.bios.2024.116298.

49. Wu, Y., Wu, M., Vázquez-Guardado, A., Kim, J., Zhang, X., Avila, R., Kim, J.-T., Deng, Y., Yu, Y., Melzer, S., et al. (2022). Wireless multi-lateral optofluidic microsystems for real-time programmable optogenetics and photopharmacology. Nat. Commun. *13*, 5571. https://doi.org/10.1038/s41467-022-32947-0.

50. Wu, M., Yang, Y., Zhang, J., Efimov, A.I., Vazquez-Guardado, A., Li, X., Zhang, K., Wang, Y., Gu, J., Zeng, L., et al. (2024). Patterned Wireless Transcranial Optogenetics Generates Artificial Perception. Preprint at bioRxiv. https://www.biorxiv.org/content/10.1101/2024.09.20.613966v1.

51. Burton, A., Obaid, S.N., Vázquez-Guardado, A., Schmit, M.B., Stuart, T., Cai, L., Chen, Z., Kandela, I., Haney, C.R., Waters, E.A., et al. (2020). Wireless, battery-free subdermally implantable photometry systems for chronic recording of neural dynamics. Proc. Natl. Acad. Sci. USA *117*, 2835–2845. https://doi.org/10.1073/pnas.1920073117.

52. Yang, Y., Wu, M., Wegener, A.J., Vázquez-Guardado, A., Efimov, A.I., Lie, F., Wang, T., Ma, Y., Banks, A., Li, Z., et al. (2022). Preparation and use of wireless reprogrammable multilateral optogenetic devices for behavioral neuroscience. Nat. Protoc. *17*, 1073–1096. https://doi.org/10.1038/s41596-021-00672-5.

53. Koebel, M., Rigacci, A., and Achard, P. (2012). Aerogel-based thermal superinsulation: an overview. J. Sol. Gel Sci. Technol. *63*, 315–339. https://doi.org/10.1007/s10971-012-2792-9.

54. Smith, D.M., Maskara, A., and Boes, U. (1998). Aerogel-based thermal insulation. J. Non-Cryst. Solids *225*, 254–259. https://doi.org/10.1016/S0022-3093(98)00125-2.

55. Kiyatkin, E.A. (2007). Brain temperature fluctuations during physiological and pathological conditions. Eur. J. Appl. Physiol. *101*, 3–17. https://doi.org/10.1007/s00421-007-0450-7.

56. Kiyatkin, E.A. (2019). Brain temperature and its role in physiology and pathophysiology: Lessons from 20 years of thermorecording. Temperature (Austin) *6*, 271–333. https://doi.org/10.1080/23328940.2019.1691896.

57. Wang, H., Wang, B., Normoyle, K.P., Jackson, K., Spitler, K., Sharrock, M. F., Miller, C.M., Best, C., Llano, D., and Du, R. (2014). Brain temperature and its fundamental properties: a review for clinical neuroscientists. Front. Neurosci. *8*, 88894. https://doi.org/10.3389/fnins.2014.00307.

58. Kim, S., Tathireddy, P., Normann, R.A., and Solzbacher, F. (2007). In vitro and in vivo study of temperature increases in the brain due to a neural implant. In 2007 3rd International IEEE/EMBS Conference on Neural Engineering (IEEE), pp. 163–166. https://doi.org/10.1109/CNE.2007.369637.

59. Kozai, T.D.Y., Jaquins-Gerstl, A.S., Vazquez, A.L., Michael, A.C., and Cui, X.T. (2015). Brain tissue responses to neural implants impact signal sensitivity and intervention strategies. ACS Chem. Neurosci. *6*, 48–67. https://doi.org/10.1021/CN500256E/ASSET/IMAGES/LARGE/CN-2014-00256E_0011.

60. Wolf, P. (2007). Thermal Considerations for the Design of an Implanted Cortical Brain,ÄìMachine Interface (BMI). In Indwelling Neural Implants: Strategies for Contending with the in Vivo Environment (CRC Press/Taylor & Francis)), pp. 63–86. https://doi.org/10.1201/9781420009309.ch3.

61. Shapiro, M.G., Homma, K., Villarreal, S., Richter, C.-P., and Bezanilla, F. (2012). Infrared light excites cells by changing their electrical capacitance. Nat. Commun. *3*, 736. https://doi.org/10.1038/ncomms1742.

62. Podgorski, K., and Ranganathan, G. (2016). Brain heating induced by near-infrared lasers during multiphoton microscopy. J. Neurophysiol. *116*, 1012–1023. https://doi.org/10.1152/jn.00275.2016.

63. Voets, T., Talavera, K., Owsianik, G., and Nilius, B. (2005). Sensing with TRP channels. Nat. Chem. Biol. *1*, 85–92. https://doi.org/10.1038/nchembio0705-85.

64. Caterina, M.J., Schumacher, M.A., Tominaga, M., Rosen, T.A., Levine, J. D., and Julius, D. (1997). The capsaicin receptor: a heat-activated ion channel in the pain pathway. Nature *389*, 816–824. https://doi.org/10.1038/39807.

65. Kang, D., Choe, C., and Kim, D. (2005). Thermosensitivity of the two-pore domain K^+ channels TREK-2 and TRAAK. J. Physiol. *564*, 103–116. https://doi.org/10.1113/jphysiol.2004.081059.

66. Koveal, D. (2024). Functional principles of genetically encoded fluorescent biosensors for metabolism and their quantitative use. J. Neurochem. *168*, 496–505. https://doi.org/10.1111/jnc.15878.

67. Pennes, H.H. (1948). Analysis of Tissue and Arterial Blood Temperatures in the Resting Human Forearm. J. Appl. Physiol. *1*, 93–122. https://doi.org/10.1152/jappl.1948.1.2.93.

68. van Erp, R., Soleimanzadeh, R., Nela, L., Kampitsis, G., and Matioli, E. (2020). Co-designing electronics with microfluidics for more sustainable cooling. Nature *585*, 211–216. https://doi.org/10.1038/s41586-020-2666-1.

69. Chen, W.-Y., Shi, X.-L., Zou, J., and Chen, Z.-G. (2022). Thermoelectric coolers for on-chip thermal management: Materials, design, and optimization. Mater. Sci. Eng. R Rep. *151*, 100700. https://doi.org/10.1016/j.mser.2022.100700.

70. Liu, H., Yang, C., and Wang, R. (2025). Passive thermal management of electronic devices. Device *3*, 100684. https://doi.org/10.1016/j.device.2024.100684.

71. Yu, W., Patros, P., Young, B., Klinac, E., and Walmsley, T.G. (2022). Energy digital twin technology for industrial energy management: Classification, challenges and future. Renew. Sustain. Energy Rev. *161*, 112407. https://doi.org/10.1016/j.rser.2022.112407.

72. Coorey, G., Figtree, G.A., Fletcher, D.F., Snelson, V.J., Vernon, S.T., Winlaw, D., Grieve, S.M., McEwan, A., Yang, J.Y.H., Qian, P., et al. (2022). The health digital twin to tackle cardiovascular disease—a review of an emerging interdisciplinary field. npj Digit. Med. *5*, 126. https://doi.org/10.1038/s41746-022-00640-7.

73. Gaikwad, A., Yavari, R., Montazeri, M., Cole, K., Bian, L., and Rao, P. (2020). Toward the digital twin of additive manufacturing: Integrating thermal simulations, sensing, and analytics to detect process faults. IISE Trans *52*, 1204–1217. https://doi.org/10.1080/24725854.2019.1701753.

74. Fang, Q., and Boas, D.A. (2009). Monte Carlo Simulation of Photon Migration in 3D Turbid Media Accelerated by Graphics Processing Units. Opt. Express *17*, 20178. https://doi.org/10.1364/OE.17.020178.

75. Deshpande, V.S., and McMeeking, R.M. (2023). Models for the Interplay of Mechanics, Electrochemistry, Thermodynamics, and Kinetics in Lithium-Ion Batteries. Appl. Mech. Rev. *75*. https://doi.org/10.1115/1.4056289.

76. Zhao, W., Liu, L., Lan, X., Leng, J., and Liu, Y. (2023). Thermomechanical Constitutive Models of Shape Memory Polymers and Their Composites. Appl. Mech. Rev. *75*. https://doi.org/10.1115/1.4056131.

77. Rodriguez, A., Zhang, H., Klaminder, J., Brodin, T., Andersson, P.L., and Andersson, M. (2018). ToxTrac: A fast and robust software for tracking organisms. Methods Ecol. Evol. *9*, 460–464. https://doi.org/10.1111/2041-210X.12874.

78. Wu, M., Minkowicz, S., Dumrongprechachan, V., Hamilton, P., and Kozorovitskiy, Y. (2021). Ketamine Rapidly Enhances Glutamate-Evoked Dendritic Spinogenesis in Medial Prefrontal Cortex Through Dopaminergic Mechanisms. Biol. Psychiatry *89*, 1096–1105. https://doi.org/10.1016/j.biopsych.2020.12.022.

79. Wu, M., Minkowicz, S., Dumrongprechachan, V., Hamilton, P., Xiao, L., and Kozorovitskiy, Y. (2021). Attenuated dopamine signaling after aversive learning is restored by ketamine to rescue escape actions. eLife *10*, e64041. https://doi.org/10.7554/eLife.64041.

80. Wu, M., Zhang, X., Feng, S., Freda, S.N., Kumari, P., Dumrongprechachan, V., and Kozorovitskiy, Y. (2024). Dopamine pathways mediating affective state transitions after sleep loss. Neuron *112*, 141–154.e8. https://doi.org/10.1016/j.neuron.2023.10.002.